POLITECNICO DI TORINO

MASTER'S DEGREE THESIS

Manipulation of topological spin textures for neuromorphic computing

---

Author:
Simone BONINO

Supervisors:
Prof. Carlo RICCIARDI
Prof. Olivier BOULLE

A thesis submitted in fulfillment of the requirements
for the Master's Degree in Nanotechnologies for ICTs

in collaboration with

Spinorbitronics Group
at SPINTEC (Grenoble)

October 15, 2024

Abstract

Simone BONINO

Manipulation of topological spin textures for neuromorphic computing

In magnetic materials, non-trivial magnetic spin textures may have topological properties, which gave them extra stability as they cannot be annihilated continuously without causing a singularity. These structures, including skyrmions, are particularly promising for applications in neuromorphic computing, where their stability and small size enable efficient information processing and storage. Other magnetic textures, such as meander domain walls, characterized by their wavy, serpentine paths due to local variations in magnetic anisotropy or material imperfections, also play a significant role in this context.

The ability to precisely control the dynamics of these structures is crucial for advancing neuromorphic computing technologies. In fact, the manipulation of domain walls can be exploited to mimic the complex, adaptive processes of the human brain.

In this context, the goal of this work is to demonstrate the potential of topological spin textures and domain walls for neuromorphic computing. Specifically, this project aims to explore the use of a magnetic system based on meander domain walls to perform reservoir computing for solving recognition tasks.

The first part focuses on optimizing material properties to stabilize meander domain walls and skyrmions in a heavy metal/ferromagnet/metal oxide system. Through careful selection of materials and device parameters, it is possible to create a system that supports these topological spin textures, which are essential for advanced neuromorphic computing applications.

The second part evaluates and measures the dynamic properties of the system. The goal is to ensure it meets the necessary requirements for reservoir computing, such as stability, non-linearity, and short-term memory, by observing the response of skyrmions and meander domain walls under various stimuli.

The final part of the manuscript is devoted to test the capability of the system to perform basic recognition tasks, with a particular focus on recognizing simple waveforms such as sine and square waves. These tests demonstrate the potential of the optimized material system for practical applications in reservoir computing, paving the way for more complex neuromorphic computing tasks in the future.

Acknowledgements

A sincere thank you to all the people who enabled me to complete this thesis work.

First of all, I would like to thank my supervisor, Professor Carlo Ricciardi, thanks to whom I discovered Spintec, the laboratory where I carried out all my research for this thesis. Thank you for your availability and for your promptness in responding to all my questions.

My special thanks go to Professor Olivier Boulle for his great professionalism and availability during my time at Spintec, his valuable suggestions, and his constant support throughout the writing of this thesis.

I would also like to thank Rodrigo and Ilaria for their patience, support, and for welcoming me from the very first moment in the best possible way. A special acknowledgment goes to all the researchers at Spintec, who, in one way or another, helped resolve all my doubts and create an excellent working environment.

I would like to thank my friends and colleagues at the Politecnico di Torino, with whom I have shared these years. It has been a pleasure studying with you, and I wish you all the best for the future. A special thanks goes to Giovanni Pedicini for being a fantastic colleague on every project.

Thanks to Giovanni, Stefano, Loris, and all my friends with whom I have shared so many years of schooling, but above all, so many unforgettable moments. Your support, despite the distance, has been invaluable.

A special thanks to my musician friends for always being there between chapters, making this journey lighter and more enjoyable with their company.

Many thanks to my family for always supporting me in every choice I made and for enabling me to get this far. To my mother, for the affection and trust she has shown me; to my father, who has been a solid and reliable presence in the most difficult decisions, from whom I have learnt a lot; and finally to my sister Sara, with whom I know I can share every fear, as well as every achievement.

Thank you all!

Ringraziamenti

Un sentito grazie a tutte le persone che mi hanno permesso di portare a termine questo lavoro di tesi.

Innanzitutto, ringrazio il mio relatore, il professor Carlo Ricciardi, attraverso il quale ho scoperto Spintec, il laboratorio presso cui ho effettuato tutte le mie ricerche per la stesura di questo elaborato. Grazie per la disponibilità e la prontezza nel rispondere ad ogni mia domanda.

Un ringraziamento particolare va al professor Olivier Boulle per la grande professionalità e disponibilità dimostratami durante la mia permanenza a Spintec, per i suoi preziosi suggerimenti e per il costante supporto nella stesura di questa tesi.

Ringrazio inoltre Rodrigo e Ilaria per la loro pazienza, il loro sostegno e per avermi accolto sin dal primo momento nel migliore dei modi. Un sentito riconoscimento va a tutti i ricercatori di Spintec, che in un modo o nell'altro hanno contribuito a risolvere ogni mio dubbio e a creare un ambiente di lavoro eccellente.

Ringrazio i miei amici e colleghi del Politecnico di Torino, con i quali ho condiviso questi anni. È stato un piacere studiare insieme a voi, e vi auguro il meglio per il futuro. Un particolare grazie va a Giovanni Pedicini per essere stato un collega di studi fantastico in ogni progetto.

Ringrazio Giovanni, Stefano, Loris e tutti i miei amici con cui ho condiviso tanti anni di scuola, ma soprattutto tanti momenti indimenticabili. Il vostro supporto, nonostante la distanza, è stato fondamentale.

Un grazie speciale ai miei amici musicisti per essere stati sempre presenti tra un capitolo e l'altro, rendendo il percorso più leggero e piacevole con la vostra compagnia.

Grazie di cuore alla mia famiglia, per avermi sempre sostenuto in ogni mia scelta e per avermi permesso di arrivare fino a qui. A mia madre, per l'affetto e la fiducia che mi ha dimostrato; a mio padre, che è stato una presenza solida e sicura nelle decisioni più difficili, da cui ho imparato molto; e infine a mia sorella Sara, con la quale so di poter condividere ogni paura, ma anche ogni traguardo.

Grazie a tutti voi!

Contents

List of Figures

List of Abbreviations

AF	**A**nti**F**erromagnet(ic)
DMI	**D**zyaloshinskii-**M**oriya **I**nteraction
DL-SOT	**D**amping-**L**ike **S**pin-**O**rbit **T**orque
DW	**D**omain **W**all
FL-SOT	**F**ield-**L**ike **S**pin-**O**rbit **T**orque
FM	**F**erro**M**agnet(ic)
GMR	**G**iant **M**agneto**R**esistance
HM	**H**eavy **M**etal
IP	**I**n-**P**lane
LLG	**L**andau-**L**ifshitz-**G**ilbert (equation)
MCA	**M**agnetic **C**rystalline **A**nisotropy
MOKE	**M**agneto-**O**ptical **K**err **E**ffect
MTJ	**M**agnetic **T**unnel **J**unction
NM	**N**on-**M**agnetic
OOP	**O**ut-**O**f-**P**lane
PCB	**P**rinted **C**ircuit **B**oard
PMA	**P**erpendicular **M**agnetic **A**nisotropy
REE	**R**ashba-**E**delstein **E**ffect
RMS	**R**oot **M**ean **S**quare
RNN	**R**ecurrent **N**eural **N**etwork
SAF	**S**ynthetic **A**nti**F**erromagnet
SHA	**S**pin **H**all **A**ngle
SHE	**S**pin **H**all **E**ffect
SOC	**S**pin-**O**rbit **C**oupling
SOT	**S**pin-**O**rbit **T**orque
STT	**S**pin-**T**ransfer **T**orque
TMR	**T**unneling **M**agneto**R**esistance

List of Symbols

A	Exchange constant	$\mathrm{J\,m^{-1}}$	
$\mathbf{D}$	Dissipation matrix	$\mathrm{kg\,s^{-1}}$	
D	DMI constant	$\mathrm{J/m^2}$	
$\mathbf{F}$	Force	$\mathrm{kg\,m/s^2}$	
$\mathbf{G}$	Gyrotropic vector	$\mathrm{kg\,s^{-1}}$	
g	Landé factor		
$\mathbf{H}$	Magnetic field	$\mathrm{A\,m^{-1}}$	
J	Current density	$\mathrm{A/m^2}$	
K_d	Dipolar energy constant	$\mathrm{J/m^3}$	
K_{eff}	Effective anisotropy constant	$\mathrm{J/m^3}$	
K_s	Surface anisotropy constant	$\mathrm{J/m^2}$	
K_u	Uniaxial anisotropy constant	$\mathrm{J/m^3}$	
$\mathbf{M}$	Magnetization vector	$\mathrm{A/m^2}$	
$\mathbf{m}$	Reduced magnetization vector		
M_s	Saturation magnetization	$\mathrm{A\,m^{-1}}$	
$\mathbf{N}$	Demagnetizing tensor		
p	Skyrmion polarity number		
Q_{sk}	Topological charge		
S	Spin quantum number		
$\mathbf{T}$	Reduced torque	$\mathrm{s^{-1}}$	
t	Thickness	m	
$\mathbf{u}$	Spin current density	$\mathrm{A/m^2}$	
$\mathbf{v}$	Velocity	$\mathrm{m\,s^{-1}}$	
$\mathcal{W}$	Winding number		
α	Magnetic damping		
α_R	Rashba coefficient	$\mathrm{J\,m^{-1}}$	
γ_0	Gyromagnetic ratio	$\mathrm{Hz\,T^{-1}}$	
δ	Domain wall width	m	
θ_{SH}	Spin Hall angle		
θ_{skHA}	Skyrmion Hall angle		
$\boldsymbol{\mu}$	Magnetic moment	$\mathrm{Am^2}$	
σ_{DW}	Domain wall energy	$\mathrm{J/m^2}$	
Ψ	Helicity number		
e	Electron charge	$1.602176634 \cdot 10^{19}$	C
m_e	Electron mass	$9.10938356 \cdot 10^{-31}$	kg
μ_B	Bohr magneton	$9.274009994 \cdot 10^{-24}$	$\mathrm{J\,T^{-1}}$
μ_0	Vacuum magnetic permeability	$4\pi \cdot 10^{-7}$	$\mathrm{H\,m^{-1}}$

Introduction

Spintec, acronym for “SPINtronique and TEchnologie des Composants”, is a leading research laboratory in spintronics. This laboratory combines fundamental research with innovative device technology in the evolving field of spin electronics.

Spintronics represents an innovative frontier, it improves conventional semiconductor technologies by addressing their limitations. Traditional semiconductor devices are nowadays close to the limits outlined by Moore’s law, in particular most of the challenges are related to power dissipation and energy consumption. Spintronics offers many advantages, including enhanced speed, storage density, and energy efficiency. Key discoveries in this field include the giant magneto-resistance (GMR) effect, tunnel magneto-resistance (TMR), spin-transfer torque (STT) and spin-orbit torque (SOT) mechanisms. Recently, the emergence of magnetic skyrmions (a type of quasi-particle magnetic spin configuration), has changed this field even more.

Skyrmions are small, topologically stable magnetic textures, with sizes ranging from nanometers to micrometers. They can be easily controlled via electric currents through spin-orbit torque. This makes them highly suitable for non-volatile magnetic memory and logic devices. Spintec was the first to directly observe skyrmions at room temperature and demonstrate their rapid manipulation (over 1 km/s) using synthetic antiferromagnetic (SAF) structures. These properties open up possibilities for high-speed, energy-efficient information storage and processing.

In addition to skyrmions, complex magnetic textures such as meander domain walls offer multiple advantages for spintronic applications. Their intricate shapes and dynamics, which can be manipulated by external fields or currents, make them promising for information encoding and processing, and for unconventional computing applications like reservoir computing.

Reservoir computing shifts computation into a nonlinear physical material, leaving only the readout to be trained. This approach enables fast learning and low training costs, yet it can still handle tasks like speech and image recognition, as well as chaotic time-series prediction. Skyrmions and meander domain walls are ideal candidates for such systems, merging the advantages of spintronics with ultra-low power recognition of complex tasks.

This work explores how non-trivial magnetic spin textures can be exploited to advance in neuromorphic computing technologies.

The first goal is to optimize an ultrathin multilayer that stabilizes complex magnetic domain wall structures at room temperature due to its unique properties. This multilayer enables skyrmion nucleation and it is suitable for magneto-optical Kerr effect (MOKE) microscopy. The research then aims to leverage its stability, nonlinearity, and memory properties for efficient reservoir computing. Several attempts are made to test simple classification tasks and analyze their accuracy. The final part of the work addresses new solutions to improve reading speed and accuracy.

In this thesis, each section addresses an important part of the research:

- Chapter 1 explains the theory of magnetism and domain walls;
- Chapter 2 explores neural networks and reservoir computing, discussing their relevance to this study;
- Chapter 3 describes the processes involved in device nano fabrication, detailing how the final device is produced;
- Chapter 4 presents the results obtained, discusses their significance, and outlines future directions for the research.

Chapter 1

Theory of magnetism

1.1 Magnetic materials

Magnetic materials are a particular class of materials, their interaction with a magnetic field leads to a change in their state that is called magnetization. There are strongly and weakly magnetic material and their interplay with a magnetic field depends on their internal structure and properties. Among them there are ferromagnetic, paramagnetic, antiferromagnetic and ferrimagnetic materials. Thus, this section is focused on the origin of material magnetic properties describing interactions and energies involved with special attention for ferromagnetic materials.

1.1.1 Magnetic moments

In order to understand the origin of magnetic properties of materials the physical description of the electronic motion must be taken into account. Specifically, at the atomic scale, a magnetic moment $\boldsymbol{\mu}$ originates from the interplay of two elements such as the spin of the electrons, that makes it behave as a small magnet, and their orbital motion around the nucleus which also generates a magnetic field.

The magnitude of the magnetic moment determines the strength of a material response to a magnetic field, while its direction indicates the orientation of the material magnetic dipoles. The magnitude of the $\boldsymbol{\mu}$ is related to the strength of the response of the material to a magnetic field, its direction describes the dipole orientation of the material. In general, these magnetic moments contribute to the overall material magnetic properties. The magnetization of a sample in a unit of volume can be written as:

$$\mathbf{M} = \frac{\sum_{i=1}^{N} \boldsymbol{\mu}_i}{V} \tag{1.1}$$

1.1.2 Ferromagnetic materials

Ferromagnetic materials exhibit a spontaneous magnetization even in absence of an applied field (spontaneous magnetization), due to particular interactions inside the material, all the magnetic moments lie locally along a single direction. These regions within the material where the atomic magnetic moments are oriented along the same direction are called domains. Common ferromagnetic materials are Iron, Cobalt and Nickel. An important aspect to take into account when dealing with ferromagnetic material is the Curie temperature T_C. In fact, above a specific temperature, different for every material, the thermal energy can overcome the natural alignment of magnetic moments causing a random orientation of the magnetic moments and the material loses its ferromagnetic properties.

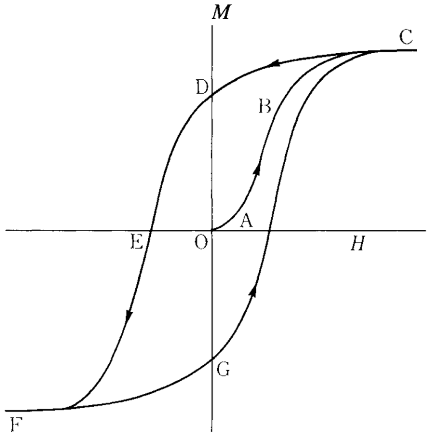

FIGURE 1.1: **Hysteresis loop** [1]

Ferromagnetic material can reach strong magnetization, however the relation between the magnetization and the applied field in complex and non linear, as shown in Fig1.1 (path OABC). It exists a field limit (point A) under which the magnetization can be reversed coming back to zero when the field is switched off. Further increasing the field, causes the magnetization to reach a plateau also called saturation M_S. Then by decreasing the magnetic field, starting from the previous saturation condition, the magnetization **M** follows another path (C to G) and at zero applied field the magnetization will not be zero. This effect is called residual magnetization or remanence. To reach a zero magnetization, the applied field must be increased in the negative direction. The intensity of the external applied magnetic field to reduce the magnetization of a ferromagnetic material to zero after saturation is called coercivity [1].

Further increase of the magnetic field in the negative sense induces the material to reach negative saturation (point F) with all magnetic moments oriented in an opposite way with the respect to the positive saturation configuration. Reversing the field another time, along the positive direction, the magnetization will follow a similar path (FEDC) forming a closed loop. Such loop is called hysteresis loop and can be exploited both for material studies but also for device applications.

1.2 Magnetic interactions

In this work thin films of ferromagnetic and non-magnetic materials are considered, therefore in order to understand the complex behaviour of a ferromagnetic-based system, we must introduce all the interactions to which the sample can be subjected, all of them can be depicted by their associated energy.

1.2.1 Zeeman interaction

When an external magnetic field is applied, the internal magnetic moments of a ferromagnetic material will be forced to follow the same direction of the external field. This interaction is referred to as Zeeman interaction. To this interaction it can be associated an energy of the type :

$$E_Z = -\boldsymbol{\mu} \cdot \mathbf{H}_{ext} \tag{1.2}$$

where $\boldsymbol{\mu}$ is the magnetic moment vector and $\mathbf{H}_{ext}$ the external magnetic field. In this case it is trivial to see that the parallel configuration is the one that minimizes the energy. Such formula describes the energy associated to a singular magnetic moment $\boldsymbol{\mu}$. To compute the total energy of the system it is sufficient to consider the sum of the individual Zeeman energies for all the magnetic moments in the material.

$$E_Z = -\int_V \mathbf{H}_{\text{ext}} \cdot \mathbf{m} \, dV \tag{1.3}$$

with $\mathbf{m}$ the reduced magnetization (normalized by the saturation magnetization M_s, $\mathbf{m} = \mathbf{M}/M_s$) .

1.2.2 Magnetic dipolar interaction

The magnetic dipolar interaction describes the energy associated with the mutual interaction of the magnetic fields generated by each dipole $\boldsymbol{\mu}_i$ within a material, separated by a certain distance $\mathbf{r}$. It takes the form of a Zeeman type interaction, and its associated magnetostatic energy can be expressed as:

$$E_d = \frac{\mu_0}{2} \int_V \mathbf{M} \cdot \mathbf{H}_d \, dV \tag{1.4}$$

Where $\boldsymbol{M}$ is the magnetization, H_d is the demagnetizing field (or stray field) generated by the magnetization itself and the factor $\frac{1}{2}$ is introduced to avoid counting the interactions between two magnetic moments twice.

Calculating this energy density analytically for each system is challenging due to its complexity, as it depends on multiple factors, is non-local, and has a long-range dependence. However in our case the main focus is oriented toward thin film magnetic samples.
Therefore considering a uniformly magnetized thin film, the relation between the demagnetizing field and the magnetization can be expressed by the demagnetizing tensor $\mathbf{N_i}$:

$$H_{d,i} = -\mathbf{N_i} M_i \tag{1.5}$$

where $i = x, y, z$, and $N_x + N_y + N_z = 1$. In such films, typically $N_x < N_y \ll N_z$ and $N_z \approx 1$ [2]. In the absence of any other anisotropic effects, the magnetization tends to align along the length of the film, which minimizes the dipolar energy. Any deviation from this alignment increases the dipolar energy, introducing a shape-induced anisotropy.

Consequently, the magnetostatic energy is minimized when the magnetization lies within the plane of the sample. If the magnetization is uniform and forms an angle θ with the normal to the thin film, the demagnetizing field simplifies to $\mathbf{H_d} = -\mathbf{M_z}$, and the dipolar energy density can be rewritten as:

$$\varepsilon_d = -\frac{1}{2}\mu_0 M_s^2 \cos^2\theta = K_d \cos^2\theta \tag{1.6}$$

Here, K_d is the dipolar energy constant or shape anisotropy constant, defined as $K_d = \frac{1}{2}\mu_0 M_s^2$. This constant represents the maximum energy density associated with demagnetizing fields [3].

1.2.3 Exchange interaction

Heisenberg introduced the concept of the exchange interaction in 1928 to explain the strong molecular fields present in ferromagnetic materials. In order to explain this phenomenon, a quantum mechanical approach is required; however, a simple description can still be given.

According to the Pauli exclusion principle, when two atoms with unpaired electrons are close to each other, their behaviour depends on the orientation of their spins, resulting in two possible scenarios: if the spins are antiparallel, the electrons can share the same orbit, thus increasing the electrostatic Coulomb energy. In contrast, when the spins are parallel, the Pauli exclusion principle forces the electrons to occupy separate orbits, which reduces the Coulomb interaction [1].

Using an atomistic description, the Hamiltonian assumes the following structure:

$$\mathcal{H}_{ex} = -\sum_{i<j} J_{ij} \boldsymbol{\mu_i} \cdot \boldsymbol{\mu_j} \tag{1.7}$$

where J_{ij} is the exchange integral between two neighbouring atoms on sites i and j. The sign of J then determines the magnetic ordering, if $J > 0$, the ferromagnetic (FM) state is energetically preferred, with all spins aligned parallel. Conversely, when $J < 0$, the antiferromagnetic (AF) state becomes energetically favored, which is characterized by neighboring spins aligning anti-parallel, resulting in zero net magnetization [3].

Considering the continuous approximation used in micromagnetism, the energy related to the exchange energy can be written as

$$E_{ex} = A \int_V (\nabla \mathbf{m})^2 dV \tag{1.8}$$

with $\mathbf{m}(r) = \frac{\mathbf{M}}{M_s}$ the reduced magnetization vector, $A \approx JS^2 \frac{n}{a}$ the exchange constant, in which a is the lattice parameter, S the spin quantum number and n the number of atoms per unit cell [4].

1.2.4 Magnetic anisotropy

The energy of ferromagnetic materials depends also on the relative orientation of the magnetization and the crystal axes. Such dependence arises from the spin-orbit coupling (SOC) inside the material. The SOC describes the relativistic interaction between the electron spin and orbital angular momenta. This energy can be described considering two main types: magneto-crystalline anisotropy energy, that is directly related to the crystal lattice of the material, and induced magnetic anisotropy energy, which result from deviations in symmetry of the system.

The MCA energy density expression may change depending on the crystal structure considered, in our case we consider the case of uniaxial anisotropy. The MCA energy density can be expressed as [5]:

$$\varepsilon_{MC} = K_{u1} \sin^2 \theta + K_{u2} \sin^4 \theta \tag{1.9}$$

where $K_{u1,u2}$ are the uniaxial anisotropy volume constants (Jm^{-3}) and θ is the angle between anisotropy axis and magnetization direction. The axis, along which the spins preferentially align, is referred to as "easy axis", while any crystallographic axis perpendicular to it is called "hard axis". Considering a ferromagnet, the energy associated with magnetization along the easy axis is minimized, reflecting a stable state of the system. In contrast, the hard axis is the direction in which magnetization is more difficult to achieve, requiring a significantly stronger magnetic field to reach saturation.

An additional form of anisotropic energy was introduced by Néel [6], known as magnetic surface anisotropy. This type of anisotropy is introduced to describe surface magnetization phenomena that are more enhanced in presence of thin film materials. In a structurally isotropic material, it can be expressed to first order as:

$$E_s = \int_S K_s[1 - (\boldsymbol{m} \cdot \hat{n})^2] dS \tag{1.10}$$

where $\hat{n}$ represents the unit vector normal to the surface and K_s the surface anisotropy constant (Jm^{-2}) [5]. For positive values of K_s, the surface energy E_s is minimized when the magnetization is perpendicular to the surface.

In bulk materials, the influence of surface anisotropy is usually negligible because the surface magnetization is strongly coupled to the bulk magnetization through exchange interactions. These effects become pronounced in very thin films and multilayer structures, where surface interactions are stronger. This balance between different contribution can be seen by considering the effective anisotropy constant K_{eff} which can be written as the summation of bulk contribution, surface contribution and shape anisotropy which has the form of a dipolar field.

$$K_{eff} = K_u + \frac{K_s}{t} - \frac{\mu_0 M_s^2}{2} \tag{1.11}$$

In thin films the term K_u can be neglected and if the interface anisotropy outweighs the shape anisotropy ($K_{eff} > 0$), the energy landscape promotes an out-of-plane easy axis, giving rise to perpendicular magnetic anisotropy (PMA). It is possible to define a critical thickness t_c above which the magnetization preferencially lines in the film plane (Fig.1.2), therefore it defines the transition between perpendicular-magnetic anisotropy (PMA) and in-plane anisotropy (IP) [3].

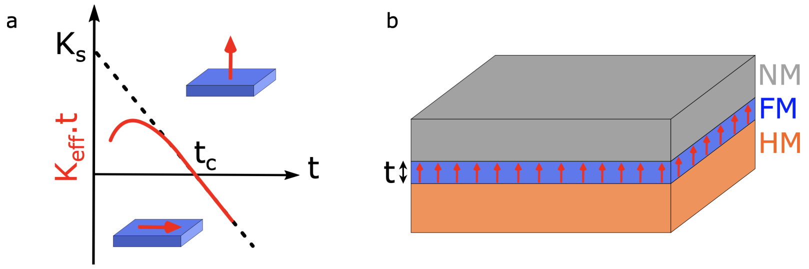

FIGURE 1.2: **Perpendicular Magnetic Anisotropy**: a. Variation of the effective anisotropy constant as a function of ferromagnetic (FM) film thickness t. In the case of Pt/Co/MgO, the critical thickness is approximately $t_c \approx 1$ nm. b. A typical PMA stack consists of a heavy metal (HM), a ferromagnetic (FM) layer, and a non-magnetic (NM) layer, such as an oxide or another heavy metal. [3]

In addition to PMA, in magnetic materials, especially in multi-layered films, the SOC gives rise to many other different phenomena such as the spin-Hall effect, the Rashba-Edelstein effect and the Dzyaloshinskii-Moriya interaction [7].

1.2.5 Dzyaloshinskii-Moriya interaction (DMI)

The Dzyaloshinskii-Moriya interaction (DMI) is an anti-symmetric exchange interaction term that appears when materials with spin-orbit coupling and inversion asymmetry are taken into account. It is crucial to stabilize chiral magnetic textures as chiral domain walls, skyrmions etc.
Firstly was proposed by Dzyaloshinskii in 1958 [8], who discovered that there was a direct link between crystal symmetry and magnetic configuration. Later in 1960, Moriya demonstrated how to compute this additional exchange term [9, 10]. The DMI Hamiltonian can be written as follows:

$$\mathcal{H}_{DMI} = -\sum_{i<j} d_{ij} \cdot (\boldsymbol{\mu_i} \times \boldsymbol{\mu_j}) \tag{1.12}$$

With d_{ij} the DMI vector (Fig. 1.3), its amplitude it is proportional to the SOC and its direction depends on the crystal symmetry [3].

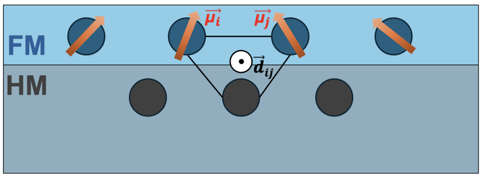

FIGURE 1.3: **Dzyaloshinskii-Moriya Interaction at the HM/FM Interface**: Schematic illustration of the DMI occurring at the interface between a HM and a FM.

1.3 Magnetic domains and domain walls

1.3.1 Origin of magnetic domains

Considering a ferromagnetic material, a magnetic domain indicates a region inside the sample where the magnetization in uniformly aligned. This division in substructures helps explain the ferromagnetic response under external magnetic fields. The reason why domain are forming is to minimize the overall system energy which is subject to many different contributions including the exchange energy, magnetostatic energy (or stray field energy), and anisotropy energy.

The concept of magnetic domains emerged from the fact that a uniformly magnetized state would produce a significant stray field energy as a large portion of the closed magnetic field would extend outside the sample [11]. By dividing into domains, the material reduces its magnetostatic energy. Furthermore, in presence of an external magnetic field, the boundaries between these domains, called domain walls, move adjusting the magnetization of the material without requiring the simultaneous rotation of all the spins.

1.3.2 Domain walls in thin films

As said before, a domain wall is the transition layer between two domains with different magnetization directions. Along the wall, the magnetization is subjected to a rotation from the direction of one domain to the direction of the other.

Specifically the magnetization along a domain wall undergoes a rotation (Fig. 1.4) which, depending on the rotation plane, can be categorized as Bloch domain wall (in the DW plane) or Néel domain wall (perpendicular to the DW plane).

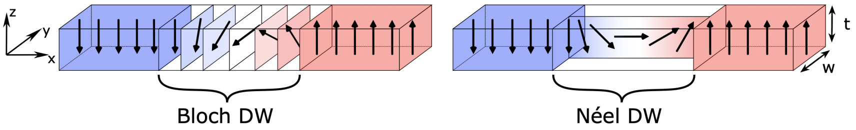

FIGURE 1.4: **Bloch and Néel Domain Walls**: Schematic depiction of a Bloch domain wall and a Néel domain wall in an ultra-thin film with thickness t and width w, displaying perpendicular magnetic anisotropy (PMA) [3].

In this section, magnetic domains and domain walls are described, with a focus on ultra-thin films exhibiting perpendicular magnetic anisotropy (PMA).

Films with strong perpendicular anisotropy are characterized by a preferred magnetic easy axis that is perpendicular to the surface of the film. To achieve this condition the material parameter Q, expressed as $Q = \frac{K_u}{K_d}$ must be greater than 1. Since $K = K_s/t$ is inversely proportional to the thickness of the sample, the surface anisotropic term promotes PMA in thin films [5].

The formation of a domain wall requires a cost in terms of energy, it is the result of the competition between two terms: the exchange energy that tends to unwind the wall and make it bigger and anisotropy energy that tends to shrink the domain wall.

By finding the equilibrium configuration in a two-spin system separated by a Block domain wall, the width of the Block wall can be expressed as [4]:

$$\delta = \pi S \sqrt{\frac{2J}{Ka}} \tag{1.13}$$

with J the exchange constant that quantifies the strength of the interaction between two neighboring spins, K the surface anisotropy constant and a the lattice parameter. Larger values of J promote thicker domain walls, while larger values of K result in thinner walls. In term of the parameter A that can be defined for different crystal lattices, the domain wall thickness can be rewritten as:

$$\delta = \pi S \sqrt{\frac{A}{K}} \tag{1.14}$$

Finally the energy per unit area can be expressed as:

$$\sigma_{BW} = \pi \sqrt{AK} \tag{1.15}$$

In the multilayer system examined in this study, the Dzyaloshinskii-Moriya interaction (DMI) is also present. Including the DMI energy contribution to the problem is equivalent to add an effective magnetic field inside the DW and perpendicular to it. Therefore a system with large DMI outweights the gain in dipolar energy of the Bloch configuration promoting Néel configuration. The domain wall energy can then be written as [12]:

$$\sigma_{DW} = 4\sqrt{(AK)} \pm \pi D \tag{1.16}$$

The sign ± distinguishes between the two possible chiralities of the Néel DW. Therefore the DMI contribution controls which configuration is favoured between Bloch and Néel and it controls also the direction of rotation of the spins inside the DW (chirality). Different thresholds can be distinguished D_N and D_C, when $D_N < D < D_C$, a pure Néel DW is stabilised while when $D > D_C$, the DW energy becomes negative and a spin spiral is stabilised, that is the magnetisation rotates continuously [12, 3].

1.3.3 Skyrmions

Other complex magnetic textures examined in this work include magnetic skyrmions. Magnetic skyrmions are unique whirling spin structures that form in certain magnetic materials due to a combination of exchange interactions and spin-orbit coupling. Their magnetic moments are topologically protected, meaning that the spin configuration is stable and difficult to annihilate or unwind. They were defined by Tony Skyrme who proposed in the 1960's a quantum field theory in order to describe interacting elementary particle as topological solitons, representing stable particle-like solutions in field theories [13].

The skyrmion whirling structure is depicted by the topological charge Q_{sk} [14, 15]

$$Q_{sk} = \frac{1}{4\pi}\int\int dxdy\, \mathbf{m}\cdot(\frac{\partial \mathbf{m}}{\partial x} \times \frac{\partial \mathbf{m}}{\partial y}) \tag{1.17}$$

with **m** the reduced magnetization vector.

In a polar coordinate system, the topological charge can be rewritten as:

$$Q_{sk} = p \cdot \mathcal{W} \tag{1.18}$$

with

$$p = \frac{1}{2}[m_z(0) - m_z(+\infty)] = \pm 1 \tag{1.19}$$

where p is the polarity number and it corresponds to the orientation of the magnetization m_z, and $\mathcal{W}$ is the winding number that counts how many times the magnetization wraps the unit sphere.

Moving outwards from the skyrmion core along the radial direction, the spins complete a 2π rotation and the specific spin rotation direction is indicated by the sign of $\mathcal{W}$, differentiating skyrmions ($\mathcal{W} = +1$) and anti-skyrmions ($\mathcal{W} = -1$). Thus, the topological charge of a skyrmion is quantized and solely determined by its core polarity.

Another quantity describing the skyrmion configuration is the helicity number Ψ and it represents the angle between the magnetization and the radial axis (r_{ij}). $\Psi = \frac{1}{2}\pi, \frac{3}{2}\pi$ refers to Bloch skyrmions, $\Psi = 0, \pi$ refers to Néel skyrmions (Fig 1.5), while intermediate values represent mixed configurations. Each skyrmion type (Bloch/Néel) can have two different polarities ($p = \pm 1$) and two different chiralities (left/right-handed).

DMI interaction is required for the generation of Bloch and Néel type skyrmions. In particular, when the DMI vector d_{ij} is parallel to the radial axis r_{ij}, Bloch type

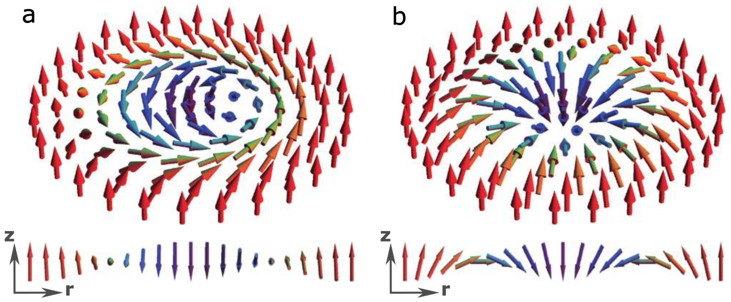

FIGURE 1.5: **Spin texture of a magnetic skyrmion**: a. A Bloch skyrmion with core polarity $p = -1$, winding number $\mathcal{W} = 1$, and helicity $\Psi = \pi/2$ (right-handed). b. A Néel skyrmion with $p = -1$, $\mathcal{W} = 1$, and $\Psi = \pi$ (right-handed). [3]

skyrmions are energetically favored, while when d_{ij} is perpendicular to r_{ij}, Néel type skyrmions are preferred [3].

1.4 Domain wall dynamics

1.4.1 Landau-Lifshitz-Gilbert equation

In order to describe and understand domain wall dynamics, it is essential to introduce the Landau-Lifshitz-Gilbert (LLG) equation which describes the spatial and temporal evolution of the magnetization [11, 16].

$$\frac{d\mathbf{M}}{dt} = -\gamma_0 \mathbf{M} \times \mathbf{H}_{\text{eff}} + \frac{\alpha}{M_s} \mathbf{M} \times \frac{d\mathbf{M}}{dt} \tag{1.20}$$

where $\gamma_0 = g|e|2m_e$ is the gyromagnetic ratio, with g the Landé factor ($g \approx 2$), e the electron charge, m_e the electron mass and $\alpha > 0$ the magnetic damping parameter. $\mathbf{H}_{eff}$ is the effective magnetic field that includes all the interactions such as exchange, anisotropy, Zeeman, external field and DMI and $\mathbf{M}$ is the magnetization vector. In the right-hand side of the the LLG a sum of two torques contributions (Fig. 1.6) is present, $\frac{d\mathbf{M}}{dt} = \mathbf{T}_p + \mathbf{T}_d$.

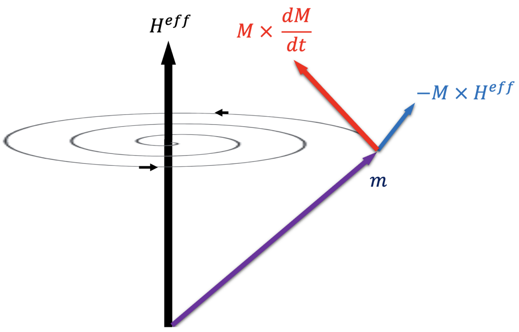

FIGURE 1.6: **Magnetization dynamics described by the LLG equation**: the term in blue is T_p and represents the precessional motion of the magnetization $\mathbf{M}$ around the effective magnetic field $\mathbf{H}_{\text{eff}}$. The second term T_d (in red) corresponds to the damping torque, which acts to align $\mathbf{M}$ with $\mathbf{H}_{\text{eff}}$.

In particular, the first term $\mathbf{T}_p$ is a conservative torque that is related to the precession of the magnetization around $\mathbf{H}_{eff}$. The second term $\mathbf{T}_d$ is a damping term perpendicular to the first one and it promotes the alignment of the magnetization with $\mathbf{H}_{eff}$ by describing a spiral around it while preserving the magnetization norm constant.

1.4.2 Current-induced domain wall motion

The manipulation of domain walls through current can be achieved thanks to two interesting phenomena: Spin Transfer Torque (STT) and Spin Orbit Torque (SOT). Both these effects are characterized by a transfer of spin angular momentum from a current to the magnetization of the sample.

Spin transfer torque

The spin transfer torque is a process in which a spin-polarized current flows through a ferromagnetic material. The oriented spins of the current acts on the magnetization and their angular momentum is transferred to the magnetic moments forcing a reorientation. STT requires a spin polarized current which is usually generated by a current that flows perpendicularly to a FM/NM/FM system in which the first FM layer is pinned and acts as a polarized.

In order to take account of this effect is the LLG modelisation for a uniform magnetization, an additional term T_{STT} must be included in the formulation [17].

$$\frac{d\mathbf{M}}{dt} = -\gamma_0 \mathbf{M} \times \mathbf{H}_{\text{eff}} + \frac{\alpha}{M_s} \mathbf{M} \times \frac{d\mathbf{M}}{dt} + \mathbf{T}_{STT} \tag{1.21}$$

Since only the perpendicular projections of the magnetization of the pinned layer onto the magnetization of the second layer give rise to a torque, the term $\mathbf{T}_{STT}$ can be written as the summation of two orthogonal components : a damping-like torque ($\mathbf{T}_{DL}$) and a field-like torque ($\mathbf{T}_{FL}$), adapted from the formulation in [18]

$$\frac{d\mathbf{M}}{dt} = -\gamma_0 \mathbf{M} \times \mathbf{H}_{\text{eff}} + \alpha \frac{\mathbf{M}}{M_s} \times \frac{d\mathbf{M}}{dt} + \frac{\tau_{\text{DL}}}{M_s} \mathbf{M} \times (\mathbf{M} \times \hat{s}) + \tau_{\text{FL}} (\mathbf{M} \times \hat{s}) \tag{1.22}$$

Where $\hat{s}$ is the unit vector that represents the direction of the spin polarization of the current and τ_{DL} and τ_{FL} are two scaling factors associated to the depicted torques, they depend on the spin current, polarization efficiency, and the magnetic properties of the material considered.

In order to describe STT in a more complex system where the magnetization is non-uniform and domain walls are present, the term T_{STT} is expressed differently taking account of two contributions: adiabatic and non-adiabatic [17].

$$\mathbf{T}_{STT_{DW}} = \mathbf{T}_{ad} + \mathbf{T}_{non-ad} = -(\mathbf{u} \cdot \nabla)\mathbf{M} + \frac{\beta}{M_s} \mathbf{M} \times ((\mathbf{u} \cdot \nabla)\mathbf{M}) \tag{1.23}$$

where the spin current density $\mathbf{u} = \frac{g\mu_B \mathcal{S}}{2eM_s}\mathbf{J}$, with $\mathcal{S} = \frac{n_\uparrow - n_\downarrow}{n_\uparrow + n_\downarrow}$ as the spin polarization of the current and J as the electrical current density (opposite to electron flow) and β is a dimensionless coefficient representing the strength of T_{non-ad}.

The adiabatic torque occurs when conduction electron spins perfectly follow the local magnetic moments within the domain wall, aligning the moments with the electron spins. The non-adiabatic term, similar to a dissipative torque, is attributed to spin-relaxation effects within the DW and is introduced to explain the observed DW velocities, which were much lower than predicted by the adiabatic term alone. Additionally it exists a critical depinning current density $\mathbf{u}_c$ that must be reached to initiate DW movement [19, 20, 21, 22, 23] (as cited in [3]).

Spin orbit torque

Spin orbit torque (SOT) phenomenon describes the torque generated on the magnetization of a sample by a current flowing across the sample. Such behaviour arises from the interplay of the interaction between the lattice and the electron orbital, the orbital and the spin, and the spin and the magnetization. Two main effects have been proposed to explain the generation of SOT: the spin Hall effect (SHE) and the Rashba-Edelstein effect (REE).

SHE is originated in the bulk of an heavy metal. When a charge current J flows through the heavy metal layer, the spin-orbit coupling causes a deflection of conduction electrons based on their spin, with electrons of opposite spins being deflected in opposite directions. The result is a pure spin current J_S that flows perpendicular to the charge current. This spin current is propagating moving from the bulk of the HM towards the HM/FM interface. The transfer of spin angular momentum to the local magnetic moments near the interface exerts a torque on the magnetization.

On the contrary, REE occurs mostly in systems with structural inversion asymmetry such interfaces and thin films. Under this effect, conduction electrons experience a Rashba field, B_R, perpendicular to their motion, aligning their spins with it and generating a non-equilibrium spin density. This spin density exerts a torque on the magnetization through the s-d exchange interaction.

SOT model For both cases (SHE and REE), the generated SOT can be decomposed into two main contributions: the damping-like SOT and the field-like SOT, respectively T_{DL} and T_{FL}. More precisely, these torque perpendicular to the magnetization can be expressed in terms of their effective magnetic fields $\mathbf{H}_{DL}$ and $\mathbf{H}_{FL}$ such that :

$$\mathbf{T}_{SOT} = -\gamma_0(\mathbf{M} \times \mathbf{H}_{DL}) - \gamma_0(\mathbf{M} \times \mathbf{H}_{FL}) \tag{1.24}$$

In general, both SHE and REE can provide damping-like and field-like contribution to the total applied torque. However, depending on the considered magnetic system, there will be a major contribution between them. In the case treated in this work, a multilayer composed by a heavy metal, a ferromagnet and a non-magnetic material is considered. Considering the specific materials involved, the SHE is expected to provide a stronger contribution to the DL-SOT while the Rashba effect is expected to provide a stronger contribution to the FL-SOT.

Therefore the main contribution for the SHE can be expressed in term of the effective damping-like field $\mathbf{H}_{DL}$ as ([24] mentioned in [3]) :

$$\mathbf{H}_{DL} = H^0_{DL}((\hat{\mathbf{z}} \times \hat{\mathbf{j}}) \times \mathbf{M}) \tag{1.25}$$

where $\hat{z}$ in perpendicular to the HM/FM interface and $\hat{j}$ is the unit vector in the direction of the current density $\mathbf{J}$, such that $\mathbf{J} = J\hat{j}$, and $H^0_{DL} \propto \theta_{\mathrm{SH}} J$ where θ_{SH} is the spin Hall angle (SHA) [25]. The SHA, defined as the ratio of spin current to charge current, indicates charge-to-spin conversion efficiency in heavy metals ($\theta_{\mathrm{SH}} > 0$ for Pt, $\theta_{\mathrm{SH}} < 0$ for Ta and W). The direction of the DL-SOT is influenced by the sign of θ_{SH} and the magnetization orientation, which affects domain wall motion in relation to the current direction [3].

For the REE the main contribution to the torque acts like a magnetic field and can be expressed as:

$$\mathbf{H}_{FL} = H^0_{FL}(\hat{\mathbf{z}} \times \hat{\mathbf{j}}) \tag{1.26}$$

with $H^0_{FL} \propto \alpha_R J$ and α_R being the Rashba coefficient. Such field acts perpendicular to the current direction and with an amplitude proportional to the current density [3].

SOT and skyrmions : Skyrmion Hall effect

Considering a skyrmion system where SOT is applied through current, this leads to a specific phenomenon known as the Skyrmion Hall effect, which causes the skyrmion to deviate laterally from the current flow direction. The system can still be modeled by the LLG equation, incorporating the additional T_{SOT} term in the context of a skyrmionic magnetic texture. However, by treating the skyrmion as a rigid configuration (no deformation), the LLG equation can be simplified. The trajectory of the skyrmion center of mass and its velocity $\mathbf{v}$ can be described by the Thiele equation [26], which is derived from the LLG equation. The Thiele equation is expressed as:

$$\mathbf{G} \times \mathbf{v} - \alpha \mathbf{D} \cdot \mathbf{v} + \mathbf{F} = \mathbf{0} \tag{1.27}$$

The term $\mathbf{G} \times \mathbf{v}$ represents the gyrotropic force (Magnus force), which arises from the topology of the skyrmion. The second term defines the dissipative force, with $\mathbf{D}$ the dissipation matrix, and α the Gilbert damping parameter. The last term $\mathbf{F}$ is related to the driving force.

The Skyrmion Hall effect can be characterized by the skyrmion Hall angle $\theta_{skHA} = \angle(\mathbf{F}, \mathbf{v})$. Since the skyrmion is treated as rigid, the steady-state velocity $\mathbf{v}$ results from the equilibrium of various forces acting on it. It is also possible to derive the expressions for the longitudinal v_x and transverse v_y skyrmion velocity (adapted from [3]):

$$v_x = \frac{\alpha D F_x - G F_y}{G^2 + \alpha^2 D^2}$$
$$v_y = \frac{G F_x + \alpha D F_y}{G^2 + \alpha^2 D^2}$$

The direction of motion is determined by the sign of F_x and F_y and it depends on the skyrmion chirality.

Recently, HM/FM-based systems have been studied for current driven skyrmion motion. In particular, it was observed that the skyrmion velocity increases monotonically with the injected current density. It was also observed that it exists a critical depinning current density below which no motion was observed which depends on the skyrmion size with 10^{10} A/m^2 for micrometer-sized skyrmions and 10^{11} A/m^2 for skyrmions with diameter around 100 nm [3].

Chapter 2

Neuromorphic Computing

In this chapter, the principles of neuromorphic computing are presented. Artificial neural networks are discussed, with a focus on recurrent neural networks. Reservoir computing is introduced as a potential alternative, and its key properties are outlined. Training methods and strategies are also addressed [1].

2.1 Principles

Neuromorphic computing working principle is based on the human brain performance. The human brain is excellent at solving pattern recognition problems, such as identifying the same person in different images despite variations in context. The ability of the brain to create consistent representations of these varied inputs is remarkable and occurs without explicit instruction. Beyond visual patterns, the brain can also recognize temporal patterns, crucial for speech recognition tasks, where the sequence of sounds is essential for understanding words. Supervised learning is key in this context; once a word is learnt, the brain can recognize it in new situations. Overall, the human brain is highly efficient in terms of speed and energy consumption at learning and recognizing patterns, outperforming algorithms, particularly in complex and variable scenarios.

2.2 Artificial Neural Networks

The initial attemps of neuromorphic computing were purely algorithmic. These algorithms are part of the larger "machine learning" field and they allow to learn, from an input data structure, an implicit rule in order to solve a specific problem. These methods can be distinguished into two main classes: unsupervised learning and supervised learning. The first one is used to solve clustering problems in which the objective is to find similarities in the input structure. The second one is instead divided into two phases: learning and inference, during the learning phases some examples are presented to the algorithm with the correct labels, then the tunable parameters of the algorithm are fixed and during the inference, new examples without the label are presented. Supervised learning includes notably support vector machine, kernel methods, and artificial neural networks [27].

The method consists of reproducing the response of a network of non-linear units (neurons) interconnected together (Fig. 2.1) with tunable connections (synapses). The neuron receives the summation of the inputs and applies to it a non-linear function called activation function such as arctan, sigmoid or rectified linear units (ReLu) (Fig. 2.2). These nodes process signals and pass them along to other nodes, forming

---

[1] This section is based on the work of [27]

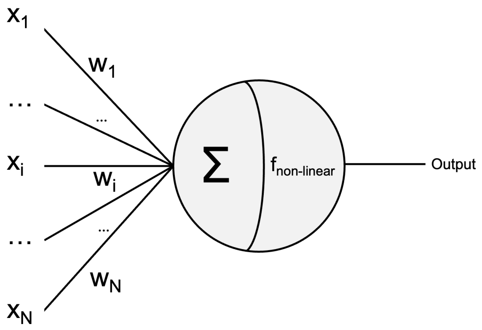

FIGURE 2.1: **Schematic of a formal neuron**: each input x_i is weighted by a connection strength w_i at the synapse. The neuron then sums these weighted inputs and applies a non-linear activation function to the resulting sum.

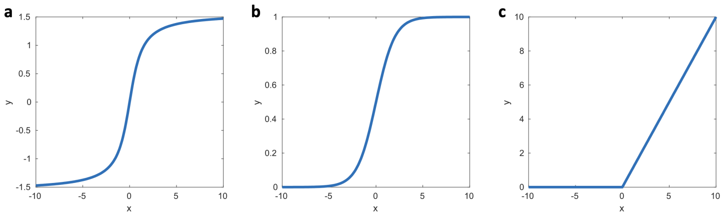

FIGURE 2.2: **Common activation functions** : a. Arctangent b. Sigmoid c. Rectified Linear Unit (ReLU).

a complex network that learns from feedback loops. The nodes are organized into layers, in fact a network with more layers is considered deeper. In artificial neural networks, the algorithm learns to solve a problem by adjusting connection weights during the training phase. Once training is complete, the weights are fixed, and the input undergoes a series of learnt non-linear transformations during the inference phase. Artificial neural networks can be categorized into two types: Feed-Forward Networks and Recurrent Networks. In this work only Recurrent Neural Networks will be considered.

2.2.1 Recurrent Neural Networks

The most suitable architectures for processing sequential data, such as sentences with multiple words or trajectories of objects in time, are recurrent neural networks (RNNs).

A recurrent neural network structure is characterized by connections between different neurons that form inner loops (Fig. 2.3) where information is circulating and thus stored. These loops give RNNs a form of memory, making them well-suited for handling information where the order of elements is crucial such as in speech recognition. However, training RNNs is generally challenging, and the training algorithm may fail to converge [28, 29]. The training process is typically performed through back-propagation algorithms and it is highly demanding in terms of computational power and time.

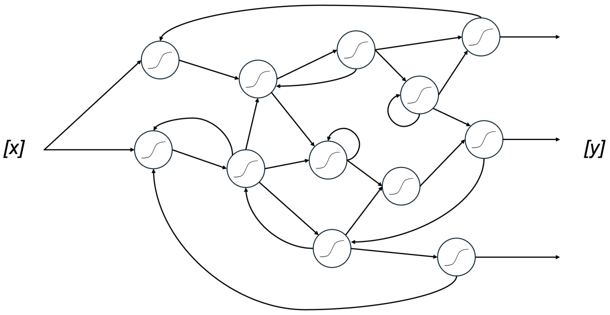

FIGURE 2.3: **Diagram of a general recurrent neural network (RNN)**

Reservoir computing offers an alternative and simpler approach with a particular type of recurrent network that does not require training the recurrent connections.

2.2.2 Reservoir Computing

Reservoir computing was introduced by Maass [30], Jaeger [31, 32] and Steil [33]. The idea behind this concept is to exploit the non-linear dynamics of recurrent neural networks for machine learning tasks. Reservoir computing can be implemented on different hardware platforms, as it requires a system that is showing a non-linear dynamical response, which can be obtained from different materials and devices.
In particular, a reservoir computing system can be divided into three different parts: input layer, recurrent network (reservoir), output layer (Fig. 2.4).

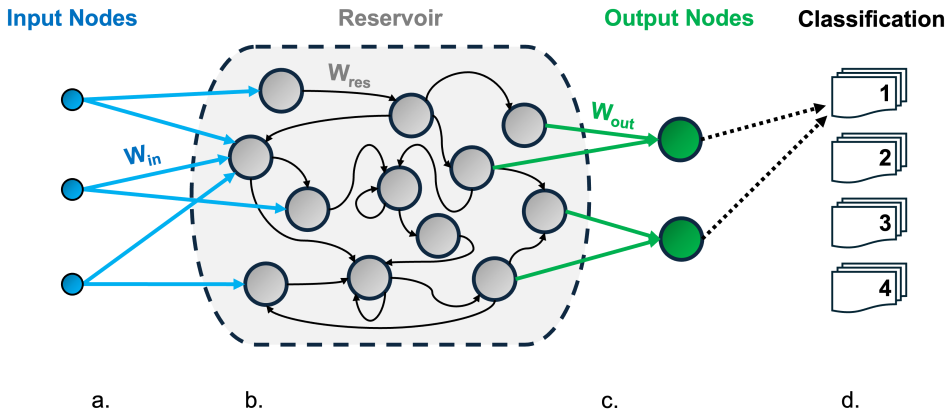

FIGURE 2.4: **Reservoir computing schematic**: the network consists of three components. The input (a) is linked to a fixed, recurrent network known as the reservoir (b), where all internal connections W_{res} are also fixed. The reservoir is then connected to the output (c) through trainable connections W_{out}. The output enables the classification of the input (d).

The first set of connections between the input layer and the reservoir and all the connection inside the reservoir are completely fixed, while only the connections between the reservoir and the output layer can be tuned according to the the specific task to be solved. Thanks to this particular characteristics, the training does not affect the properties and the dynamics of the reservoir itself. The dimension of the input and of the output data depends on the particular classification task that has to be solved. By calling $\mathbf{x}(k)$ the vector of the neuron responses of the reservoir $x_i(k)$ at time k :

$$\mathbf{x}(k) = \begin{pmatrix} x_1(k) \\ x_2(k) \\ \vdots \\ x_n(k) \end{pmatrix} \tag{2.1}$$

then the evolution of the reservoir network can be described as :

$$\mathbf{x}(k) = f_{nl}\left(\mathbf{W}_{\text{in}}\mathbf{u}(k) + \mathbf{W}_{\text{res}}\mathbf{x}(k-1)\right) \tag{2.2}$$

where $\mathbf{W}_{\text{in}}$ is the matrix containing the connection weights between the input $\mathbf{u}(k)$ and the reservoir, and $\mathbf{W}_{\text{res}}$ is the matrix containing the connection weights within the reservoir. The function f_{nl} represents the non-linear transformation performed by the neurons in the reservoir. It is important to note that the parameters $\mathbf{W}_{\text{in}}$, $\mathbf{W}_{\text{res}}$, and f_{nl} are fixed, furthermore, since the response $\mathbf{x}(k)$ depends on the particular sequence in input, it depends also on the previous input values denoted by $\mathbf{x}(k-1)$ [27]. The output $\mathbf{y}(k)$ is obtained by combining the neuron outputs $x_i(k)$ through a linear combination:

$$\mathbf{y}(k) = \mathbf{W}_{\text{out}}\mathbf{x}(k) + \mathbf{W}_{\text{bias}} \tag{2.3}$$

Here, $\mathbf{W}_{\text{out}}$ is the matrix of the connection weights between the reservoir and the output, and $\mathbf{W}_{\text{bias}}$ is a bias vector with constant values.

By defining $\mathbf{s}$ and $\mathbf{W}$ as:

$$\mathbf{s}(k) = \begin{pmatrix} 1 \\ \mathbf{x}(k) \end{pmatrix}$$

$$\mathbf{W} = \begin{pmatrix} \mathbf{W}_{\text{bias}} & \mathbf{W}_{\text{out}} \end{pmatrix}$$

The equation for the output can be simplified :

$$\mathbf{y}(k) = \mathbf{W}\mathbf{s}(k) \tag{2.4}$$

The computation is effective if a linear regression on the reservoir responses can accurately approximate the desired output. The role of the reservoir is not to solve the problem directly, but rather to transform the initial problem into one that can be solved linearly.

Properties

The general goal of a reservoir is to map the initial problem into an higher dimensional space (Fig. 2.5) in which the problem is expected to become linearly separable [34]. In this way, the problem can be solved by a linear combination of the last connection layer between the reservoir and the output, which is the only layer that can be tuned. In order to achieve this result, the reservoir system must satisfy three different properties : separability, approximation and fading memory [36, 37].

The separation property is the ability of a reservoir to produce different responses for different inputs, which is essential to obtain a linearly separable problem and it can be achieved through a high number of interconnected neurons in the reservoir.

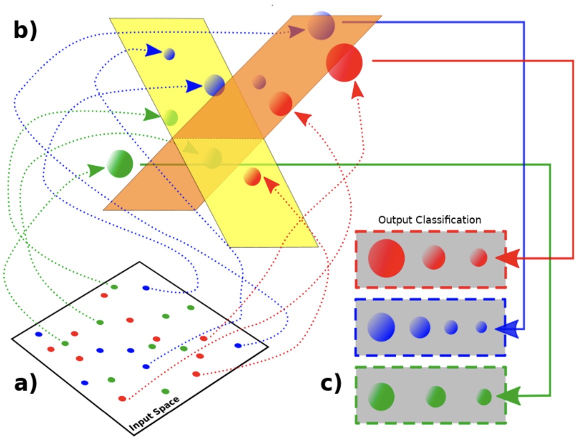

FIGURE 2.5: **Schematic of the reservoir computing operational principle**: a. Unstructured data from the input space are non-linearly transformed by the transient dynamics of the reservoir into a higher-dimensional state space. Inputs with similar correlations (represented by similar colors) lead to similar reservoir dynamics. b. A single linear regression step is then applied to define hyper-planes in the state space of the reservoir, allowing different input categories to be separated. The role of the reservoir is to project complex spatio-temporal patterns into a sparsely populated high-dimensional space, making them easier to recognize and classify (c). [35]

The higher-dimensional state of the reservoir corresponds to the responses of all neurons, where each neuron response is acting as a coordinate in this state. To achieve a higher dimensional mapping, two key requirements are necessary: having more neurons than the input dimensions and ensuring non-linear neuron behaviour to produce independent responses. This approach is similar to other machine learning techniques, but what distinguishes reservoir computing is the interconnected non-linear nodes that enables successive transformations of the input.

The approximation property ensures that similar inputs produce similar responses. Thus, the reservoir must be resilient to noise, otherwise even a slight input variation could lead to significantly different responses and incorrect classification. However the approximation property set a limitation to the separation property since too similar inputs will not be separated, therefore a trade-off between these two properties is necessary.

Fading memory refers to a short term memory of recent events. This memory is generated by internal loops within the reservoir that can store information [38]. Such property is essential for processing sequence of data that requires memory and it also depends on how far back the reservoir needs to remember in order to classify inputs accurately.

Training

Reservoir computing is a supervised learning algorithm with two main phases: training (or learning), where the neural network learns to solve a task, and testing (or inference), where it applies what it learnt to new problems. The system includes internal parameters that are adjusted during the training phase, in the case of reservoir computing specifically the output connection weights W_{res}^{out} and the bias weights W_{bias} are tuned.

The learning process relies on finding a set of parameters that minimize the error between the actual output of the neural network and the correct output. Commonly the error considered is the L2 norm of the difference between the predicted and desired outputs. This error is then normalized by the number of examples : root mean square error (RMS).

By considering the correct output $\tilde{Y}$ and the actual output Y:

$$\text{RMS} = \frac{1}{N_{\text{train}}} \|Y - \tilde{Y}\|_2 = \frac{1}{N_{\text{train}}} \sqrt{\sum_{k \in \text{training}} (y(k) - \tilde{y}(k))^2} \tag{2.5}$$

Considering $S = (s(k))$ as the reservoir state, the optimized W can be retrieved by:

$$W = \tilde{Y} S^{\dagger} \tag{2.6}$$

where † denotes the Moore-Penrose pseudo inverse [39].

Once the optimal weights are determined, the learnt parameters are evaluated on a test set. If the error is low on the training examples but high on the test set, it indicates that the neural network is overfitting to the training data.

Overfitting is a common issue in machine learning where a model performs well on training data but poorly on test data due to poor generalization and it will be translated to very large values of weights.

To mitigate overfitting, Tikhonov regularization (or ridge regression) is employed [40]. By adding a penalty term $\lambda \|W\|^2$ to the error function (with λ a small positive factor)

$$\|Y - \tilde{Y}\|_2 + \lambda \|W\|_2$$

large weight values are discouraged, promoting simpler models and better generalization. Tikhonov regularization ensures a unique optimal set of weights and helps in achieving convergence during training [27].

Chapter 3

Experimental techniques

In this chapter, all the experimental techniques used are described. In particular the first section refers to all techniques employed to fabricate the material stack and the device layout. The second section is dedicated to the techniques employed in the measurement setup.

3.1 Sample fabrication and characterization

Different combinations of heavy metals (HM), ferromagnets (FM) and metal oxides have been optimized in order to stabilize skyrmions at room temperature (RT) as in the work of Boulle et al.[41] using Pt/Co/MgO nanostructures. This stack accomplishes the required characteristics needed to stabilize skyrmions and complex domain walls: perpendicular magnetic anisotropy (PMA), Dzyaloshinskii-Moriya interaction (DMI) and a strong spin-orbit torque (SOT).

Among other material stacks, the Ta/FeCoB/TaOx/AlOx configuration has been extensively studied at Spintec [42]. One key advantage of this stack is the presence of meander domain walls and the ability to nucleate skyrmions at room temperature using a small out-of-plane (OOP) magnetic field. Due to their micrometer size, these magnetic skyrmions and domain walls can be directly observed using magneto-optical Kerr effect (MOKE) microscopy. This stack offers several benefits for non-conventional computing applications (such as reservoir computing): it provides large PMA and DMI for skyrmion and domain wall stabilization as well as a significant SOT. This frame enables low energy current induced non-linear dynamics, pointing this system as an ideal player for reservoir computing.

In this study, we investigate a Ta/FeCoB/TaOx/AlOx film, which was deposited using magnetron sputtering and then, patterned into devices with track configuration through lithography (Fig. 3.1).

3.1.1 Magnetron sputtering deposition

Magnetron sputtering deposition is a physical vapor deposition method used to coat substrates with thin films of material. The process involves a target material and a substrate placed in a chamber at room temperature under vacuum (from 10^{-6} to 10^{-9} mbar) to achieve a good quality of the deposition. A plasma is generated from an inert gas (Ar), and a DC electric field is applied between the target material and the substrate to sustain the plasma. The argon ions are then accelerated toward the target, causing atoms from the target to be ejected and deposited on the substrate, forming a thin film.

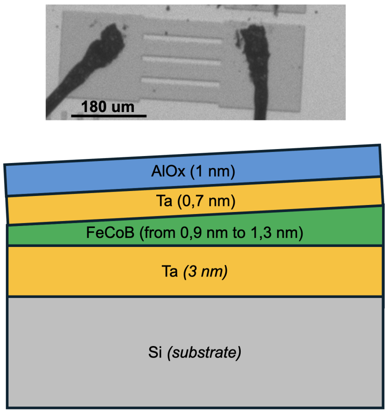

FIGURE 3.1: **Layout and composition of the device studied**: a. Parallel tracks for domain wall motion through SOT. b. Material stack with wedge deposition of the FeCoB layer.

In magnetron sputtering, a magnetic field is placed close to the target surface in order to enhance the number of ionizing collisions, in this way the efficiency and the uniformity of the sputtering process are increased.
There are two main configurations for the deposition: on-axis deposition and off-axis deposition. In the first configuration the substrate is placed under the target and set in rotation, achieving a spatially homogeneous deposition all over the sample. In the second configuration, the substrate is laterally displaced with respect to the target (Fig. 3.2) and the rotation is stopped, in this way the deposition will depend on the angle of incidence and the deposition rate will depend on the relative position to the target. In particular, when the substrate is closer to the center of the plasma, where the density of sputtered atoms is highest, the deposition rate is greater, resulting in a thicker film. On the other hand, as the substrate moves toward the edges of the plasma or farther from the target, the deposition rate decreases, leading to a thinner film.
In this work we are interested in the off-axis deposition because the magnetic properties analyzed strongly depends on the material thickness (in this case on the FeCoB thickness). This technique allows materials to be deposited as wedges, creating a thickness gradient along one direction of the substrate. As a result, a wide range of thicknesses in a given stack can be characterized on a single wafer.

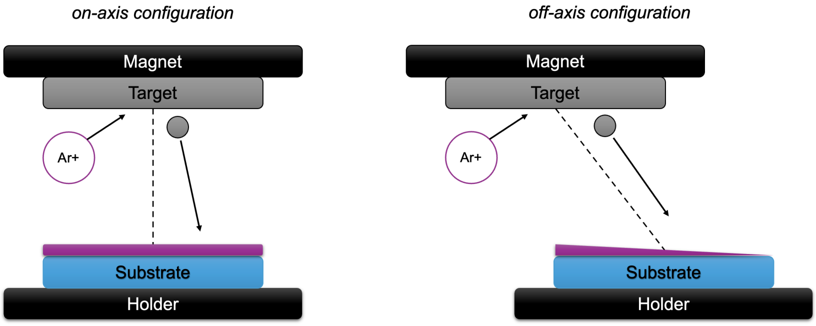

FIGURE 3.2: **Magnetron sputtering**: two possible configurations are available. In the off-axis configuration material can be deposited as a wedge with a thickness variation of up to a factor of 2 across a 100 mm wafer.

3.1.2 Stack analysis (NanoMOKE)

The Nano Magneto-Optical Kerr Effect (NanoMOKE) system measures magnetic properties by detecting changes in the polarization of light upon reflection from a magnetized surface. A polarized laser beam is reflected from the sample, and the resulting polarization rotation is analyzed to determine the local magnetization. By applying an external magnetic field and measuring the Kerr rotation at different field strengths, magnetic hysteresis loops are generated, revealing key properties like coercivity, magnetic anisotropy, and saturation magnetization. NanoMOKE is especially suited for high resolution studies of thin films due to its nanoscale measurement precision.

Before patterning the sample, prior characterization is required to ensure the desired magnetic properties. In particular, to reduce the energy required to nucleate skyrmions in structures with weak DMI, we need to operate near the spin reorientation region. In this region, the magnetic anisotropy changes, rotating the magnetization of the sample from in-plane to out-of-plane. Therefore, since the wafer is characterized by a thickness gradient in the FeCoB layer along one direction, it is possible to perform Magneto-Optical Kerr measurements in the NanoMOKE to retrieve magnetic hysteresis loops at different positions along the wedge, as shown in Fig. 3.3.

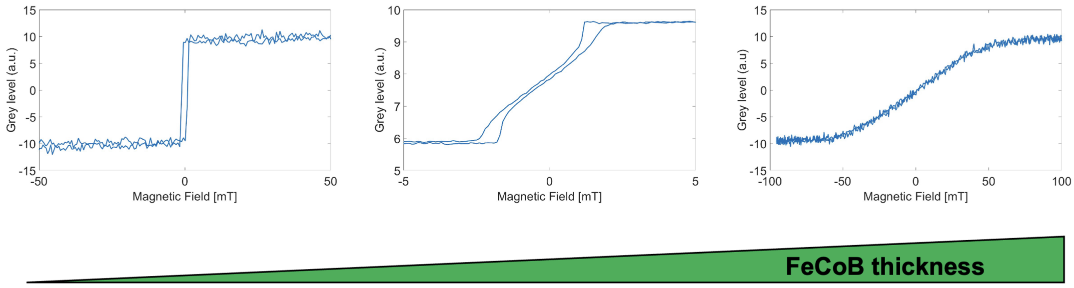

FIGURE 3.3: **Magnetic hysteresis loops based on FeCoB layer thickness**: For lower thicknesses, the hysteresis loop exhibits a square shape due to a sudden change in magnetization, as surface magnetic anisotropy drives the magnetization completely out-of-plane. As the FeCoB layer thickness increases, the magnetization is gradually confined to the in-plane direction, causing the hysteresis loop to change from an intermediate "butterfly" shape to a more linear shape.

3.1.3 Device fabrication

The sample considered in this study was fabricated through a precise series of nanofabrication processes (Fig. 3.4). After the sputtering deposition of the Ta/FeCoB/TaOx/AlOx stack on the Si/SiO_2 wafer, there is an annealing step to change the oxidation rate at the interface of the ferromagnetic layer. Then a spin coating with positive resist is performed in order to achieve the right photoresist thickness followed by a soft baking step to let the solvent evaporate.

Subsequently the wafer is exposed to laser lithography, a precision patterning technique where a laser is used to selectively expose a photosensitive material. The laser beam projects the detailed pattern in the area that has to be exposed [[1]]. After the development of the resist, the pattern is imprinted and the non-desired areas are removed.

Once the effective layout that has to be obtained is completely covered by the thick resist, an etching step is performed. In this specific case, the physical etching considered is an Ar-ion-beam etching in which a focused beam of accelerated ions is exploited to sputter material from the substrate surface. Ions are generated, accelerated, and directed towards the material, causing atoms to be ejected away from the surface in a controlled manner. The control of the different etched materials is performed by an atomic mass spectrometer inside the chamber. A final conductivity test at different wafer locations is performed to verify that the etch step has reached the silicon layer in the unprotected area.

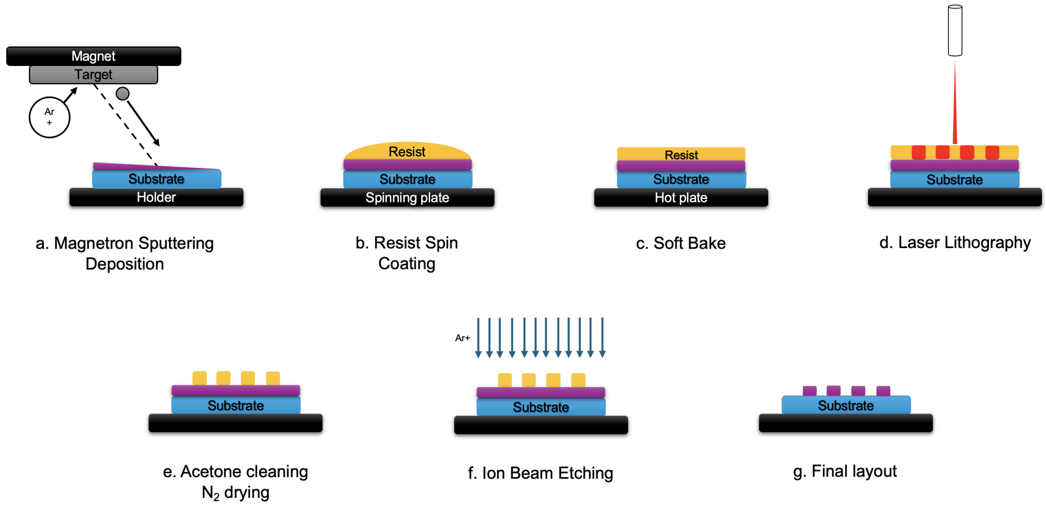

a. Magnetron Sputtering Deposition

b. Resist Spin Coating

c. Soft Bake

d. Laser Lithography

e. Acetone cleaning N_2 drying

f. Ion Beam Etching

g. Final layout

FIGURE 3.4: **Nanofabrication process**: a. Multilayer magnetron sputtering deposition with FeCoB wedge. b. Resist spin coating for uniform deposition. c. Resist bake for solvent evaporation. d. Laser lithography to create the protective mask with a thick resist layer. e. Undeveloped resist removal. f. Ion beam etching exploiting the thick resist layer as an hard mask. g. Final pattern.

3.2 Measurement setup

This section is devoted to all the measurement techniques employed for the analysis and characterization of the magnetic properties of the device under consideration.

3.2.1 Magneto-optic Kerr effect

The Magneto-optical Kerr effect (MOKE) is an optical phenomenon observed when polarized light reflects off a magnetized material. In particular, the polarization state of the light will change due to the interaction between the electric field of the incident light and the magnetization of the material. In the absence of magnetization, the

---

[1] The design of the layout and the fabrication of the device were performed by Rodrigo Guedas Garcia.

dielectric tensor of a material is typically diagonal and isotropic, meaning that it has the same value in all directions. However, when a material is magnetized, the dielectric tensor becomes anisotropic, and the dielectric tensor can be represented as a 3x3 matrix with off-diagonal elements:

$$\epsilon = \begin{pmatrix} \epsilon_{xx} & \epsilon_{xy} & \epsilon_{xz} \\ \epsilon_{yx} & \epsilon_{yy} & \epsilon_{yz} \\ \epsilon_{zx} & \epsilon_{zy} & \epsilon_{zz} \end{pmatrix}$$

Since the off-diagonal elements are non-zero, a coupling between different components of the electric field of the incident light is introduced. Upon reflection, these anisotropic changes in the dielectric properties cause a rotation of the plane of polarization (Kerr rotation) that can be described by the Kerr angle θ_K, and can also induce ellipticity in the reflected light (Kerr ellipticity). These changes depend on the relative orientation between the magnetization direction and the plane of incidence of the light. The combined effect of rotation and ellipticity alters the polarization state of the reflected light in a way that can be detected and quantified in order to retrieve the magnetization state of the studied sample.

There are three main configurations based on the orientation of the magnetization relative to the surface and the incident light (Fig. 3.5). The polar configuration occurs when the magnetization is perpendicular to the surface, making it sensitive to out-of-plane magnetization, and is often used for studying thin films or surface magnetism. The longitudinal configuration involves magnetization within the surface plane and parallel to the plane of incidence, and is used for analyzing in-plane magnetization dynamics and domain structures. Finally, the transverse configuration has magnetization within the surface plane but perpendicular to the plane of incidence, leading to changes in the intensity of the reflected light without altering the polarization plane (no Kerr rotation).

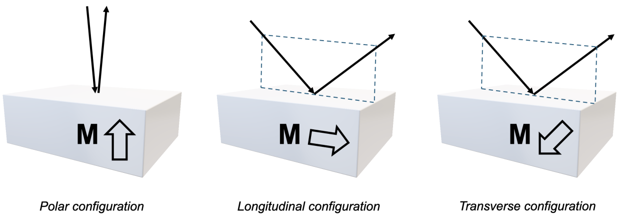

FIGURE 3.5: **Magneto-optical Kerr effect configurations**: In polar configuration, the magnetization is perpendicular to the sample surface and parallel to the plane of incidence. In longitudinal configuration, the magnetization is parallel to both the sample surface and the plane of incidence. In transverse configuration the magnetization is parallel to the sample surface but perpendicular to the plane of incidence.

For the study of the sample analyzed in this work, only the polar configuration will be considered since the device shows an out-of-plane magnetization.

3.2.2 Experimental setup

The experimental setup exploited in this work consists mainly of a MOKE microscope, a printed circuit board to hold the sample and all the electrical instrumentation to generate, apply and register arbitrary electrical current signals across the device.

The main components of the microscope are a laser source, a polarizer to linearly polarize the incident light, a set of objective lenses to focus the light on the sample, an analyzer which is crossed with the polarizer to detect Kerr rotation and a CCD camera. An electromagnet is positioned below to apply a controlled out-of-plane magnetic field. The CCD camera is automatically controlled by a program to subtract the saturated magnetic image, enhancing the contrast.

The full wafer is cut into a small piece to isolate some devices and connect them on a dedicated PCB (Fig. 3.6). In particular the wafer die is attached to the surface of the PCB with silver glue and, through an ultrasonic microwire bonding machine, a selected track is connected to the electronic setup thanks to two PCB plugs.
Current is then supplied with an arbitrary waveform generator which contains basic wave forms or eventually custom signals that can be uploaded with an USB key.
The output plug is connected to an oscilloscope in order to measure the voltage drop on the device and retrieve the current density and the width of the injected signal. When the current is flowing through the device, the CCD camera of the MOKE microscope records the response and the motion of the magnetization along the track. The recorded videos will be analyzed through a Matlab routine that was improved and made more precise in detection as part of my internship work.

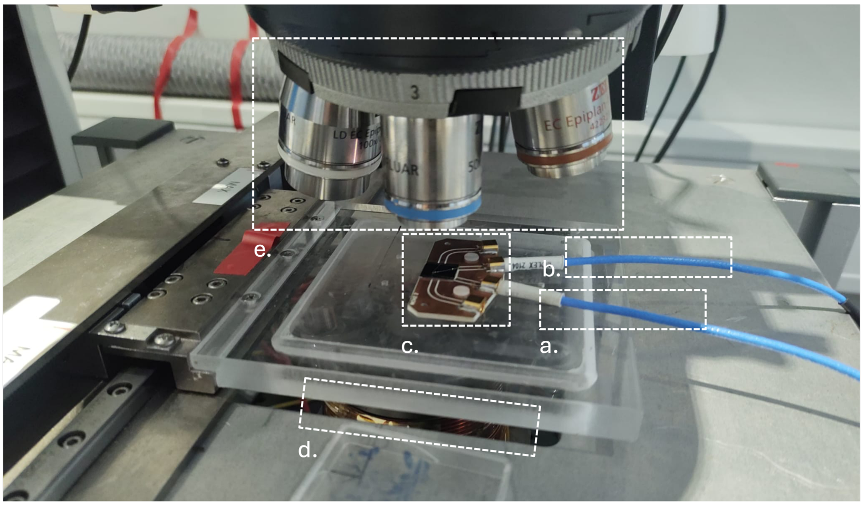

FIGURE 3.6: **Experimental Setup**: a. Input cable connected to an arbitrary waveform generator. b. Output cable for oscilloscope signal detection. c. PCB holder for the device. d. Magnetic coil for out-of-plane applied magnetic field control. e. MOKE lens system connected to a CDD camera.

3.2.3 Video processing analysis

To observe the current-driven motion of the magnetic texture, a sinusoidal current signal is delivered through the track and videos of the response are recorded. Then the videos are analyzed by an algorithm previously implemented in Matlab and improved as part of my work at Spintec (Fig. 3.7).

The code exploits the MATLAB Image Processing Toolbox to read and analyze recorded videos from MOKE experiments conducted under various current regimes. The aim of this analysis is to extract key information about the magnetic system for applications in our neuromorphic based approach.

Since the video is recorded from a real experiment, there are noise issues, particularly within the domain wall structures, where contrast fluctuations occur that should not be interpreted as motion but rather as noise. To address this, a Gaussian filter is applied to remove background noise caused by the CCD camera. This stabilizes the image, ensuring that white pixels no longer appear within the black domain walls in each frame.

To simplify motion detection, the approach is to work with a binary image. A threshold value is set to binarize the image, and then the code stores the frame at time t and compares it with the frame at $t + \tau$.

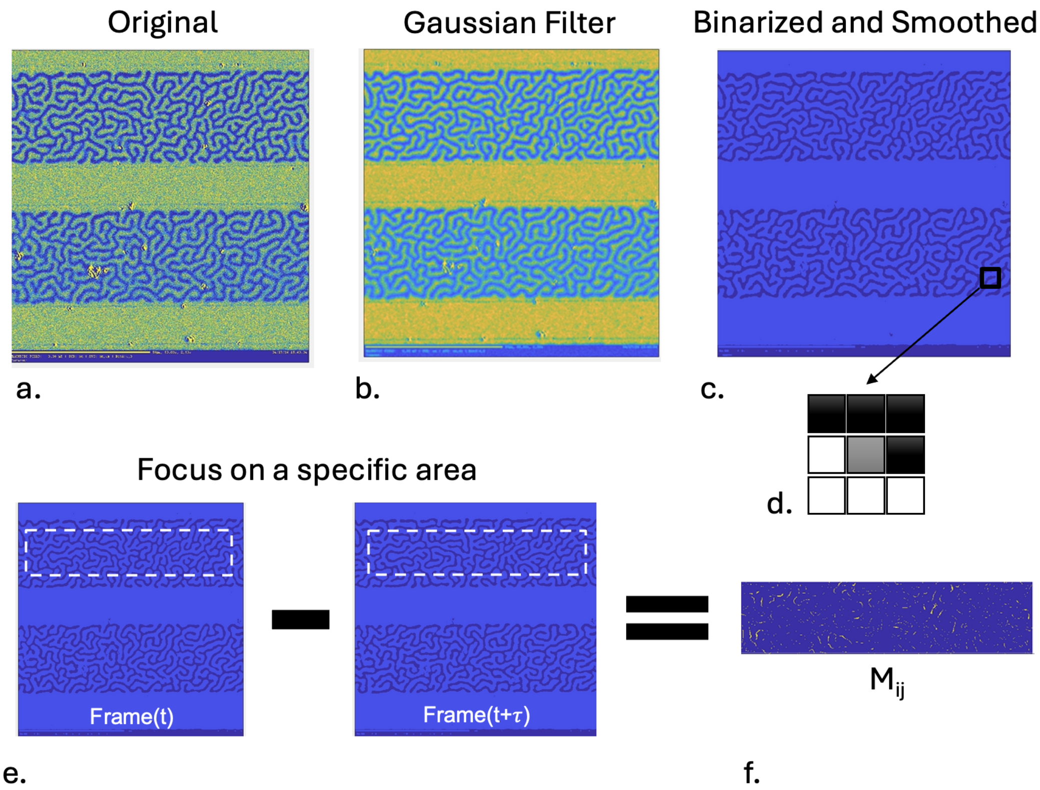

FIGURE 3.7: **Detection algorithm**: The figure illustrates all steps involved in image processing. Blue and green colors enhance clarity, representing values ranging from 0 to 1, while the yellow color results from the application of a Gaussian filter, which smooths the colors together. a. Original image is read. b. Gaussian filter is applied for noise reduction. c. Binarization of the image. d. Edge smoothing with a kernel. e. Difference of successive frames. f. Matrix storing and mean value computing.

The comparison between frames can yield various data and information. One method to quantify the movement of the magnetic texture is by calculating the direct difference between the two frames. This difference is stored in a matrix, and by averaging the values across the rows and columns, a single representative value for each time frame is obtained. The output associated to this method can be linked to the average velocity of the domains and will be referred to as the "average domain displacement", denoted as $|dX_{DW}|$, such that:

$$|dX_{DW}| = \langle\langle frame(t+\tau) - frame(t)\rangle\rangle \tag{3.1}$$

This value describes the average domain wall displacement in time.

Another possibility for the detection is to register the contrast in time, in this case each frame is stored in a matrix and a mean value is computed for each time frame t.

$$|C_{contrast}| = \langle\langle frame(t)\rangle\rangle \tag{3.2}$$

This second output can instead be associated with the change in contrast over time, which is linked to the change in magnetization of the selected area.

The results presented in the next chapter are based on measurements of the average domain displacement $|dX_{DW}|$, as these measurements provide better results with less noise issues.

Chapter 4

Results

In this chapter are presented some of the results obtained during my work at Spintec. Firstly the nucleation of meander domain walls and skyrmions at room temperature with an applied magnetic field is shown. Afterwards, domain wall dynamics is presented for different current regimes. The following section is dedicated to the study of the properties of the system required for reservoir computing : non-linearity and short-term memory. Finally some simple classification tasks (such as sine/square) are tested exploiting the magnetic system as a physical reservoir.

4.1 Domain wall nucleation

An ultrathin film of Ta/FeCoB/TaOx/AlOx is considered, deposited via magnetron sputtering onto a Si/SiO_2 substrate. After the deposition of 3 nm of Ta on the substrate to achieve high spin-orbit torque, the FeCoB wedge is deposited, whose thickness varies from 0.9 nm to 1.3 nm. On top, 0.73 nm of TaOx are deposited and finally, as a capping layer to protect the surface, 1 nm of AlOx is added. This multilayer stack was engineered to include the critical components required for stabilizing magnetic skyrmions/domain walls, specifically perpendicular magnetic anisotropy (PMA) and interfacial Dzyaloshinskii-Moriya interaction (DMI).

MOKE analysis

Since the sample considered shows different properties depending on the thickness of the ferromagnetic layer, the first part of my study is focused on the observation of different hysteresis loops along the direction where the gradient of thickness is present (Fig. 4.1). In fact, in ferromagnetic materials, the hysteresis loop characterizes the relationship between the applied magnetic field $\mathbf{H}$ and the resulting magnetization $\mathbf{M}$, and the shape of the loop reflects distinct magnetic behaviours.

In particular, for low ferromagnetic thickness, the surface anisotropy term prevales, resulting in a square hysteresis loop. A square hysteresis loop indicates materials with sharp transitions between magnetization states, where the magnetization quickly flips direction as the applied field reaches a critical value. From the viewpoint of the image seen by the MOKE, an abrupt change in contrast can be seen when the magnetic field exceeds one of two specific thresholds. Square loops are common in memory devices like MRAM, where the magnetic states must be very stable.

On the other hand, for higher ferromagnetic layer thickness, the hysteresis loop is more linear, this means that the change in the magnetization lies on the surface plane (in-plane magnetization) and the orientation changes gradually.

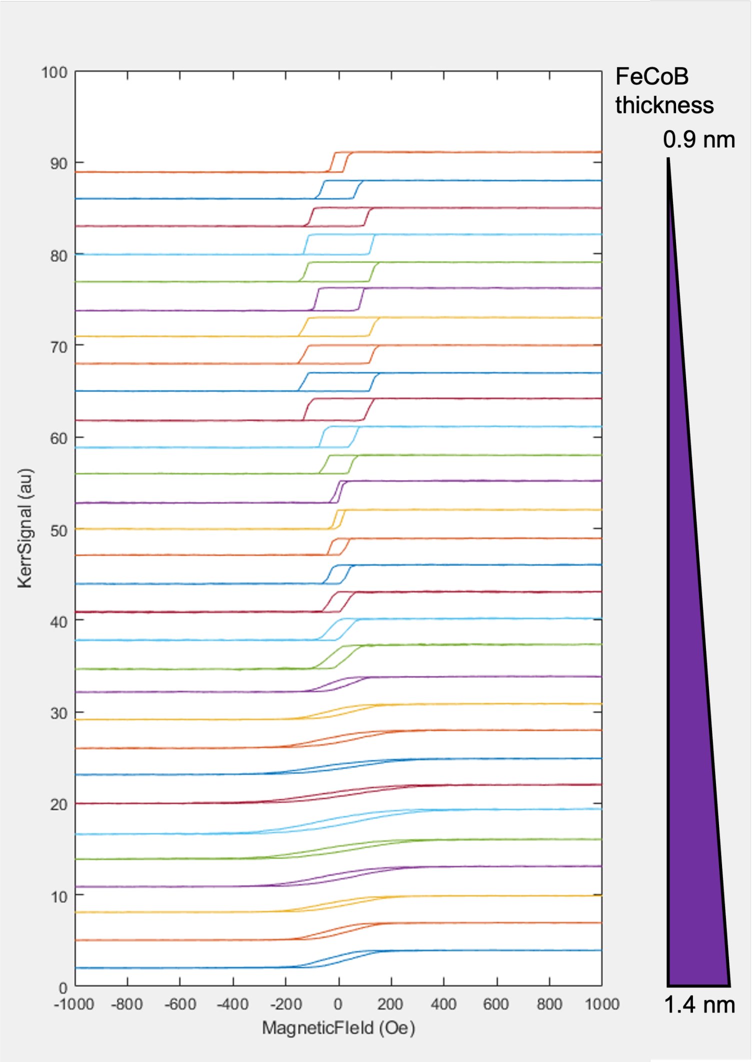

FIGURE 4.1: **NanoMOKE analysis of magnetic hysteresis loops as a function of the FeCoB film thickness**: The graph displays hysteresis loops at various spatial positions along the wedged sample, presented with an offset for clarity. The thickness of the ferromagnetic layer affects the anisotropic magnetization properties. As the layer thickness increases, the hysteresis behaviour transitions from a square loop at lower thicknesses to a more linear loop at higher thicknesses.

This can be easily checked on the MOKE image, since there is a gradual change in contrast while sweeping the magnetic field, resulting in no clearly identifiable magnetic texture.

The target in order to stabilize meander domain walls is a region where the hysteresis loop presents intermediate features, this loop is also known as "butterfly loop". This loop displays a more complex shape resembling a butterfly, with distinct regions indicating different behaviours. Butterfly hysteresis loops often involve complex magnetic domain interactions, creating an environment where magnetic structures like meander domain walls or skyrmions can emerge.

In particular, at zero applied out-of-plane magnetic field, it is possible to obtain meander domain walls (also known as stripe domains), as this configuration minimizes the demagnetizing energy. The density of stripe domains can be controlled by varying the thickness of the FeCoB layer (by moving along the wedge); the closer to the in-plane transition, the denser the texture becomes. To regulate the stripe, the application of a small magnetic field perpendicular to the sample surface is required (around 1 mT). This favors stripes with magnetization parallel to the external field, increasing their size.

Furthermore, by applying a small out-of-plane magnetic field (2.27 mT) larger than the one for stripe domains, thanks to the Zeeman interaction we can favor the alignment of domain walls toward +z or -z, thus the stripe domains will shrink eventually forming isolated skyrmions (Fig. 4.2). In this case, it is important to select a region with a high density of meander domain walls. This ensures that, as the texture shrinks due to the external field, some features in the middle of the device may remain isolated from the track edges and, during the shrinking process, can form isolated bubbles or skyrmions.

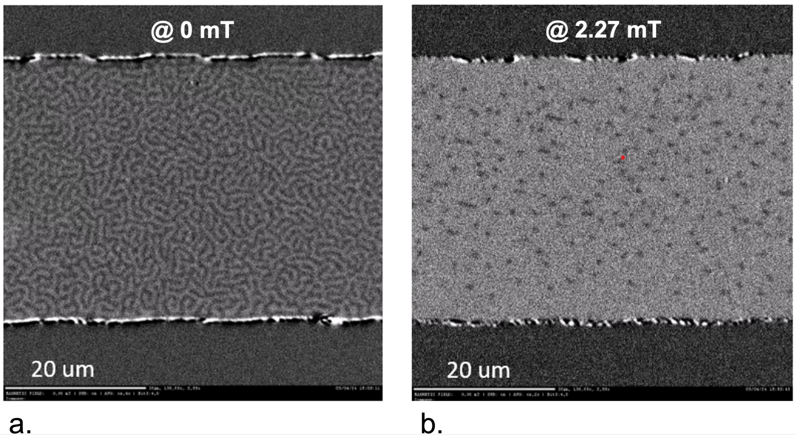

FIGURE 4.2: **MOKE image of different magnetic textures**: At ferromagnetic thicknesses around 1.1–1.2 nm, complex textures are visible. a. Meander domain walls appear without an applied magnetic field. b. Skyrmion nucleation is achieved with an applied OOP magnetic field of 2.27 mT

Once the proper region for skyrmion/stripe domains has been identified, by modifying the magnetic field it is possible to navigate different spin texture configurations in order to find the best trade-off to achieve a good quality in the detection process. From the perspective of the magnetic texture, fundamental parameters include the out-of-plane magnetic field and the thickness of the ferromagnetic layer, with the goal of achieving complex domain walls with sharp edges. From the point of view of the MOKE camera system, the key parameters are focus, frames per second (fps), and exposure time, with the trade-off aimed at maximizing resolution without significantly reducing the fps.

When the current is applied along the track, current induced dynamics will be generated due to SOTs. The behaviour of the magnetic system under this current stimulus is recorded in a video by the CCD camera of the MOKE microscope. To detect and measure the motion, a Matlab algorithm is used.

4.2 Current induced dynamics

4.2.1 Current regime optimization

Along with the optimisation of the detection code, during my work I also focused on optimising the current (pulse amplitude, pulse width) and magnetic field parameters (saturation field, working point). In particular the correct value of magnetic field is important to obtain a meander domain wall structure with sharp edges, in this way the detection is more precise when the structure is in motion. Also the parameters for the current density have to be optimized, too low current density will lead to a small displacement and a poor detection, while a too high current density leads the entire magnetic structure to severe deformation (Fig. 4.3).

Deformation presents a considerable challenge because, under these current regimes, the magnetic structure undergoes significant elongation in the direction of motion (the current direction), complicating detection. Since displacement primarily occurs along this direction, an elongated structure (Fig. 4.3) results in a reduced average displacement being detected due to the presence of parallel magnetic textures, whose motion cannot be fully captured by the algorithm.

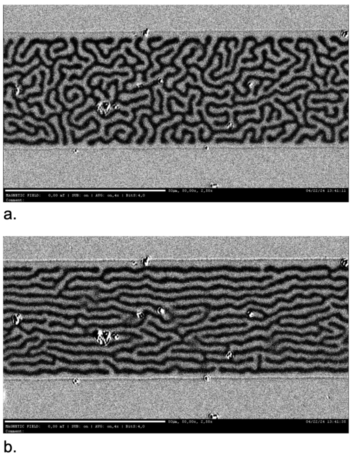

FIGURE 4.3: **Strong deformation issue**:
a. Relaxed meander magnetic texture.
b. Strong elongation after the application of a voltage of 1V for 40s.

Therefore, a compromise must be made to ensure that there is sufficient motion for detection while avoiding excessive elongation of the meander structure. The current regime examined in this work is approximately 10^{11} A/m^2.

4.2.2 Simple response test

A preliminary set of tests is conducted to understand how the system behaves and deforms under various waveforms. Initially, a DC current is applied to the sample at different voltage levels to check the detection and the evolution over time of the magnetic texture (Fig. 4.4). Key parameters observed include the existence of a threshold voltage (around 500 mV) required to generate sufficient spin-orbit torque to trigger DW depinning, as well as a general reduction in output detection at higher voltages and longer duration, likely due to the elongation of the meander texture along the track direction, as discussed in the previous paragraph.

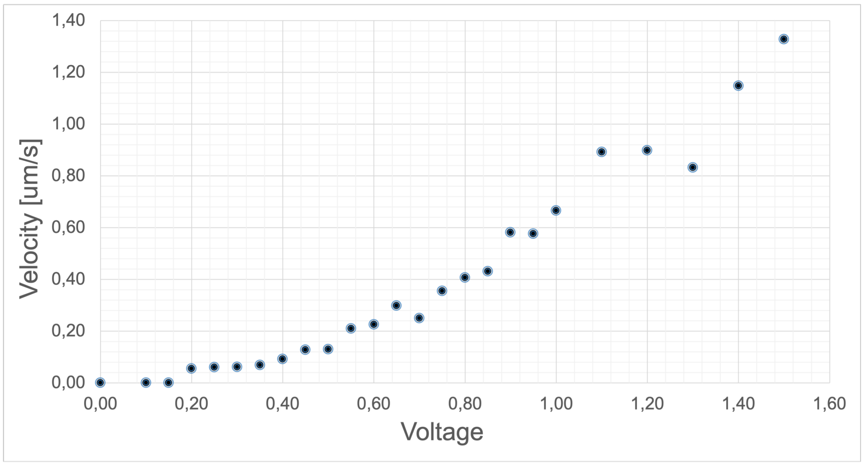

FIGURE 4.4: **Domain wall velocity as a function of the applied DC voltage**: Velocities registered at different voltage values show non linear behaviour.

Successive tests involve applying simple waveforms to determine whether the system responds differently depending on the input pattern, examining the shape of the response, and estimating whether differences can be visually distinguished (Fig. 4.5). This initial step is important to understand how diverse patterns may influence the system and to evaluate its potential suitability for reservoir computing. For this purpose, square and sinusoidal waves with a period of T = 10s and at various voltages are applied through the tracks. Once clear and distinct responses to simple patterns are achieved, the system must undergo a more detailed analysis to identify the necessary properties for neuromorphic applications.

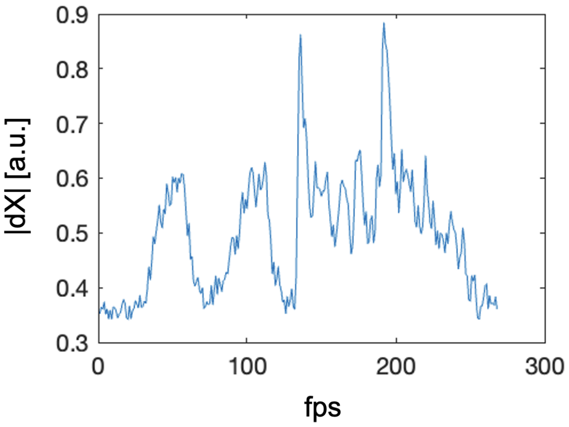

FIGURE 4.5: **System response to sine/square wave**: The graph illustrates the average domain displacement $|dX|$ as a function of frame number in response to a signal composed of a single sine wave with a period of T=10s followed by a square wave of the same period. The signal voltage amplitude is ± 800mV. Distinct responses to the two waveforms are observed: frames 40 to 140 represent the output in response to the sine wave excitation, while frames 141 to 240 depict the response to the square wave input.

4.2.3 Non Linearity of the system

As previous discussed, one of the key aspect for a physical system to be exploited for reservoir computing is the non linearity. In order to prove this concept for the meander domain wall system, a systematic study as a function of the current density is performed.

A sinusoidal current signal is applied along the device track, and the motion is recorded and analyzed by computing the average domain wall displacement $|dX|$ with the technique presented in 3.1. Then the same process is repeated for different amplitudes in order to map the behaviour of the system dynamic for different current regimes. At the end all output signals are analyzed together and their amplitude is compared in different time positions (Fig. 4.6).

What we can observe is that the response amplitude as a function of the voltage is non-linear, which is exactly the goal of this test. More in detail, there is a threshold voltage below which no motion occurs, providing clear evidence of non-linearity. At higher voltages, the behaviour becomes less abrupt. Therefore, for reservoir computing applications, we will focus on the 600 mV to 800 mV range, where non-linearity is observed. Furthermore, Fig.4.6 shows how for different time, the response is different. This can be explained by the fact that after some time the current flowing through the track is deforming the stripe domain structure, making them more elongated toward the flow direction. In this way, the average domain wall displacement in time is different since the texture is slightly different.

4.2.4 Memory properties

Another key property for a physical reservoir is short term memory. Once a system is stimulated by the same input it should in principle respond in the same way. However, if the system has internal memory, the previous input signal history will affect the output signal, in this way for the same input signal at a specific time position t it is possible to obtain slightly different dynamic response. This characteristic is fundamental to mimic the neuron behaviour in order to perform classification tasks.

The idea to test it is to apply a voltage input signal which is composed by a sequence of sine waves. In the first measurement just sine waves are applied, in the second one, a single square wave is applied before the train of sine waves [43]. The two outputs are then analyzed and compared, as shown in Fig. 4.7(a).

First, it can be observed that the system responds differently to various waveforms: for a square wave, the system exhibits two sharp peaks, each followed by a relaxation response, whereas the response to a sine wave excitation displays smoother behaviour.

After one cycle (at time t = 10 s) the system is stimulated by a sinusoidal current, however it shows two different responses depending on the previous excitation, this is what is called memory. The duration of the memory of the system can be quantified and its value is around 1.8 s for an excitation with a period of 10s.
The same process can be repeated by applying a train of square waves to the system and changing the first wave with a sinusoidal one (see Fig. 4.7). In this case, we observe that the amplitude of the response remains the same, but the two signals are offset by 0.4.

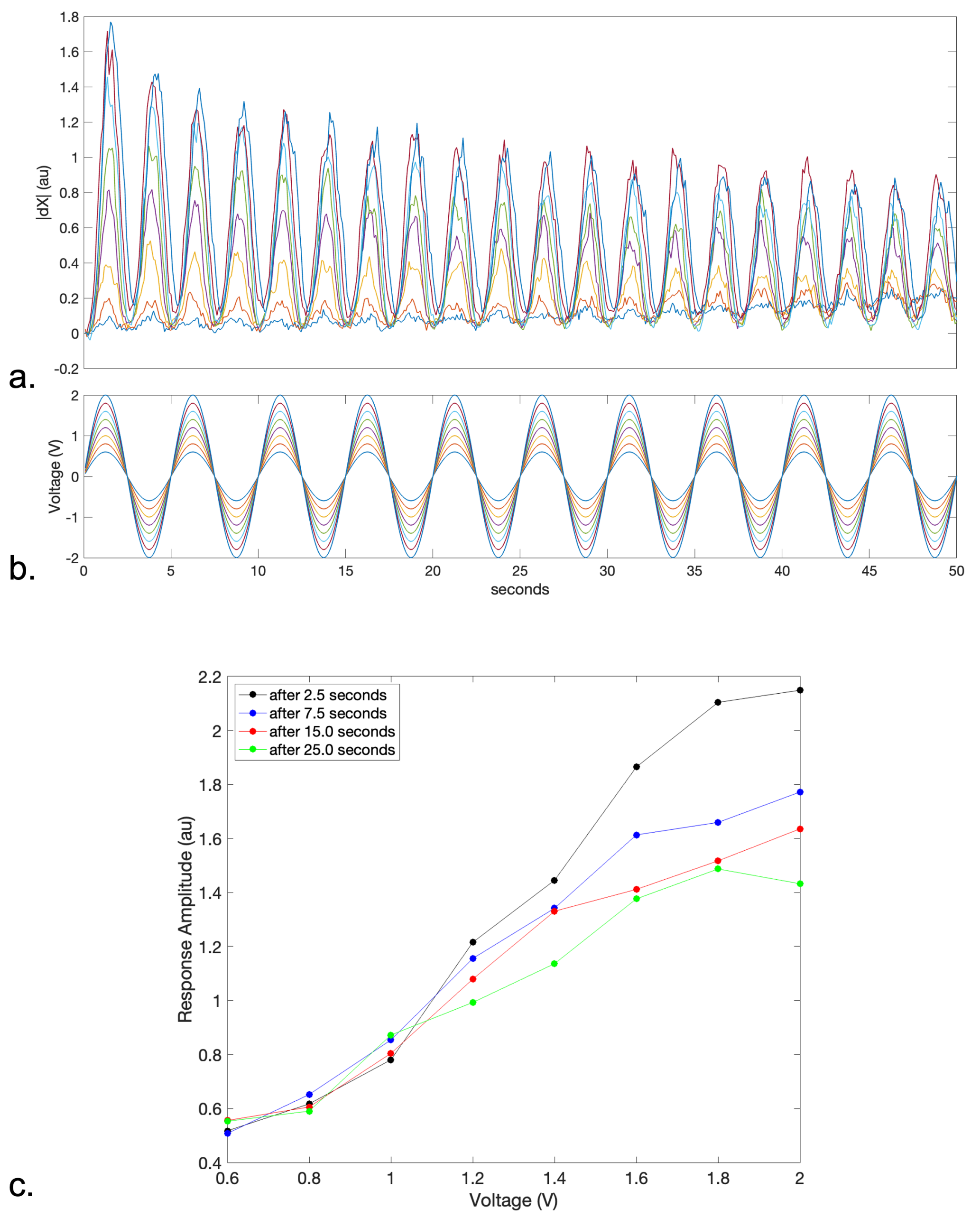

FIGURE 4.6: **Sine wave response at different voltage and Response Amplitude as a function of the applied voltage**: a. Response signal to a sine wave excitation (shown in b) as a function of time, with different colors representing responses to various input signal amplitudes. b. Input signals applied with amplitudes ranging from ±600 mV to ±2 V, all having the same period (T=5s). c. Amplitude of the response as a function of the input sine wave voltage amplitude, with different colors of the dots indicating responses at various times.

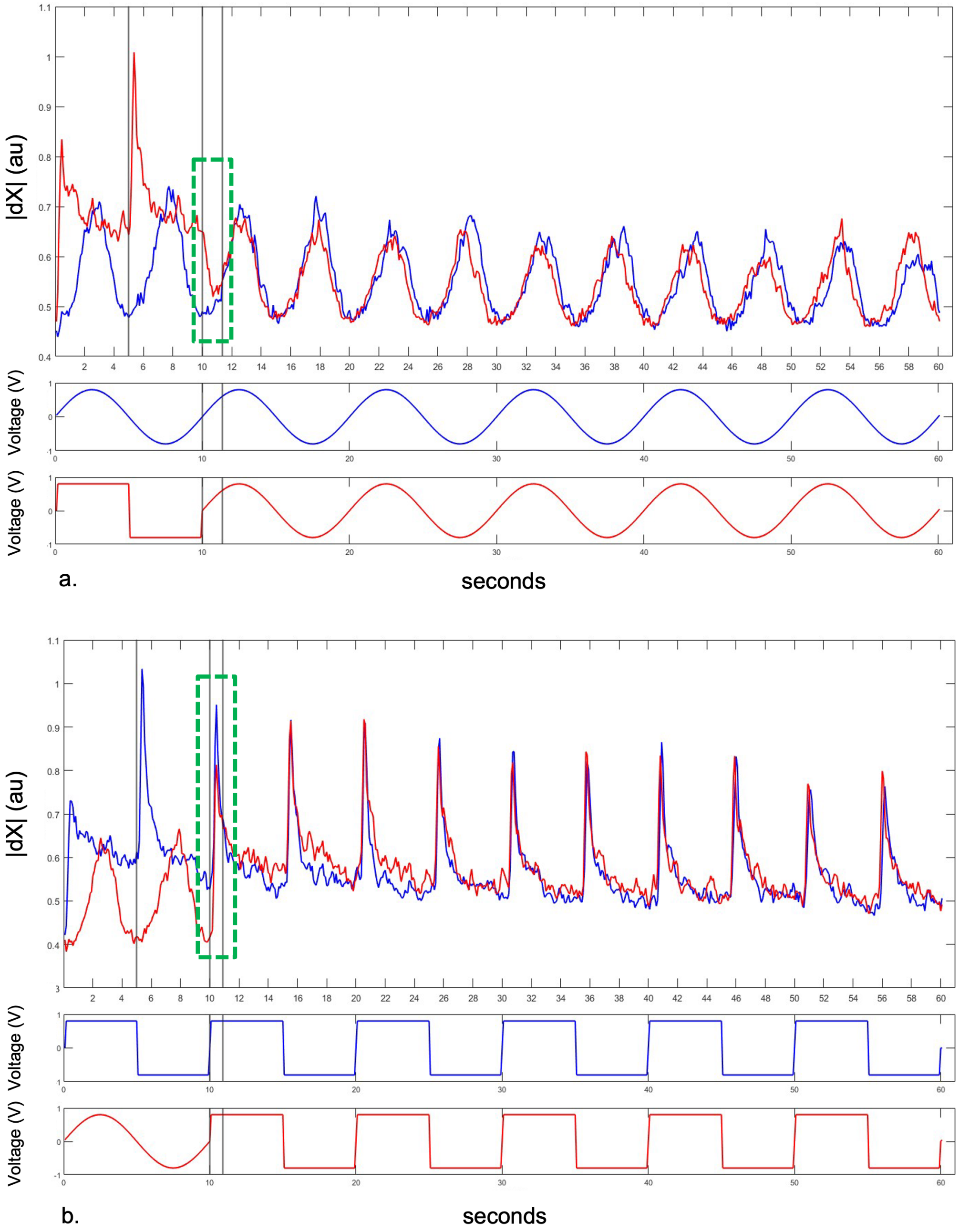

FIGURE 4.7: **Short term memory properties of a meander domain wall system**: a. A sine wave of amplitude ±800 mV and period of T=10s is applied to the system (in blue), and the average domain wall displacement $|dX|$ is measured (reported in blue). The same signal is applied again, substituting the first part of one cycle with a square wave of the same period (in red), and $|dX|$ is computed. In the dashed region (highlighted in green), despite the same applied signal, the system produces two different outputs depending on its prior excitation history. b. The same process is repeated using square wave inputs.

4.3 Towards Reservoir Computing

Since the system satisfies all the required properties, then it can be tested as a reservoir for simple recognition tasks.

The objective in this study is to differentiate sine or square. A random sequence of 80 sine/square waves is applied to the system and the response is registered and averaged over 20 different measurements. Then recorded videos are divided into multiple regions, each of them representing a single neuron with its own response. This subdivision has been done in different ways (Fig. 4.8), modifying the area considered and the number of neurons. A good trade-off between area size and the number of neurons must be found, as regions that are too small result in a magnetic texture that lacks sufficient complexity for reservoir computing, while regions that are too large reduce the number of neurons in the reservoir.

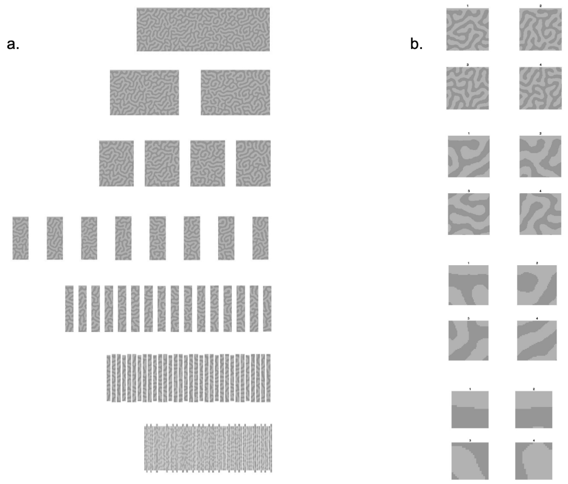

FIGURE 4.8: **Track subdivision into multiple neurons**: a. Rectangular slices subdivision for spatial reservoir computing. b. Square area subdivision within the track, showing different square lateral sizes (from top to bottom: 17 μm, 8.5 μm, 4.25 μm, and 2.12 μm).

4.3.1 Classification tasks

In order to classify the different patterns, it is necessary to train the last layer of the reservoir which is the only one that can be tailored. In particular, the input signal $u(t_k) = (v(t_1), v(t_2), ..., v(t_k))$ is transformed in a non-linear way by the reservoir and can be represented by the matrix M:

$$M = \begin{bmatrix} M^1(t_1) & M^2(t_1) & \cdots & M^N(t_1) \\ M^1(t_2) & M^2(t_2) & \cdots & M^N(t_2) \\ \vdots & \vdots & \ddots & \vdots \\ M^1(t_K) & M^2(t_K) & \cdots & M^N(t_K) \end{bmatrix}$$

Where the index i = 1:N represents the different neurons, that means different considered areas of the track, and j = 1:k represents the different time points. Then a first part of the matrix is used to train the last layer of the neural network. In the example shown, the 80% of the matrix is used to train and the remaining 20% is used for the test. The training step is quite simple since just one layer is involved and it is a linear regression:

$$y(t_k) = \sum_{i=1}^{N} W_i M^i(t_k)$$

where $y(t_k)$ is the real classification vector containing 1 for square and 0 for sine. We denote $M_{learning}$ as the 80% of M and D the 80% of the class vector y. Then to retrieve the trained value W_i we perform the following steps:

$$S = (M_{learning})^{\dagger}$$

which is the Moore-Penrose inverse, and

$$W = (S \cdot D)'$$

Finally the last part of the custom input signal is used to test the accuracy of this physical system in the recognition :

$$y_{test} = W \cdot M_{test}$$

Then, since y_{test} will be a vector containing values between 0 and 1, a binarization is forced in order to obtain a 0/1 vector that can be compared with the real classification to evaluate the accuracy.

For accuracy evaluation, different configurations are considered, varying the number of neurons from 2 to 128, doubling at each step (Fig. 4.9). Additionally, different area subdivisions are explored, such as uniform square regions across the track or parallel rectangular segments. The graph below shows accuracy as a function of the number of neurons for the rectangular subdivision. Results for the square subdivision are not included in this work due to the need for further improvements, as it is more affected by noise. We observe that the accuracy oscillates between 60% and 70%. This irregular trend arises because increasing the number of regions reduces the signal and information from each individual area, making each signal more susceptible to noise.

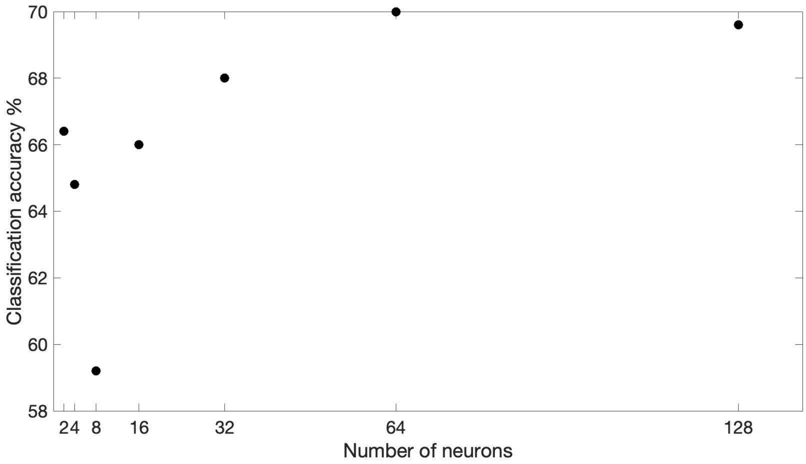

FIGURE 4.9: **Classification accuracy**: Classification accuracy is reported as a function of the number of neurons considered for a rectangular area subdivision.

The accuracy achieved in this task is relatively low. In contrast, similar magnetic texture systems, such as the skyrmionic one described in [43], have demonstrated accuracies of up to 90% for the same classification task. Several factors may contribute to this disparity. For instance, measurement noise degrades tracking precision, which lowers recognition accuracy. Moreover, the correlation plots from different regions of the physical system exhibit an almost linear behaviour (see Fig. 4.10), meaning that each neuron is too similar to all the others. This lack of differentiation in their responses limits accurate classification and suggests that the system may not possess the necessary complexity for reliable performance.

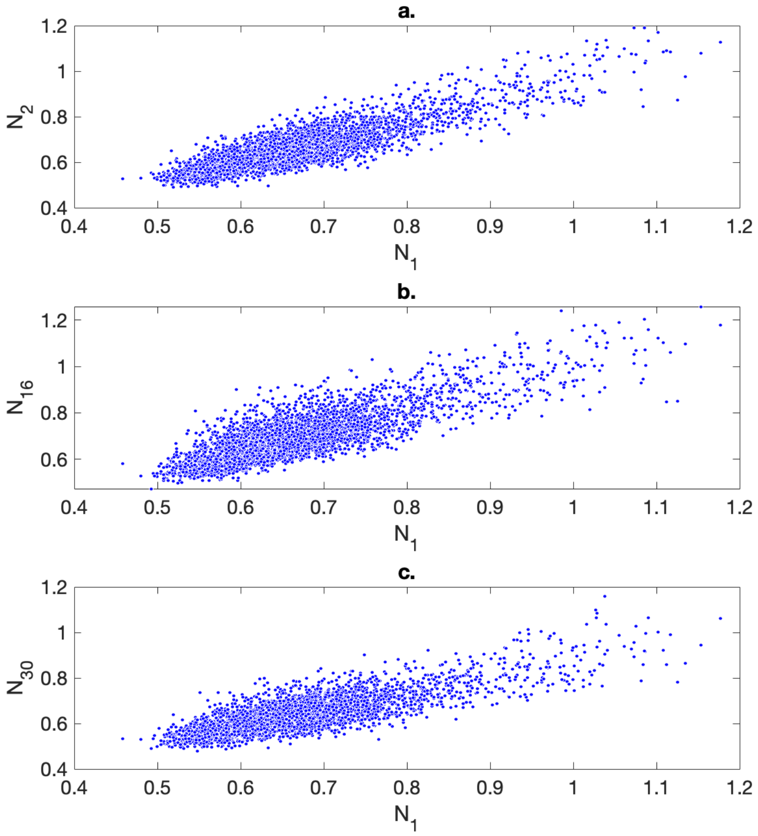

FIGURE 4.10: **Correlation plots of different neurons** : a.b.c. The graph illustrates the average domain wall displacement $|dX|$ for neuron 1 as a function of $|dX|$ for other neurons: N2 (a), N16 (b), and N32 (c), which are positioned at different locations along the track.

4.4 Improvements and Outlooks

As previously discussed, this particular complex spin texture system can be exploited as a physical reservoir to perform simple classification task. However the recognition accuracy must be enhanced to be reliable. To this task, I started to work on some new solutions to obtain a much more complex system that shows different responses depending on the spatial position of the neuron considered.

Several tests were conducted to investigate whether a different current density across various regions of the track induce a non-linear correlation among the neurons. Specifically, a non-patterned sample with the same material stack was used to inject current. In the absence of tracks, a higher current density is observed near the contact region, while a lower density is found farther away. The average domain wall displacements for each region are measured and compared. The general observation is that the correlation becomes less linear compared to previous configurations.

Then to exploit this phenomenon, the first idea is to change the layout of the device in order to achieve a different current density distribution along the track (Fig. 4.11). In this way, different positions will be subjected to different current densities for the same applied signal. Since each region can be associated with a neuron, this configuration results in a more differentiated set of neurons, enhancing the capability and accuracy of the system in classification tasks by providing access to more information.

Two main layouts have been designed and fabricated : a notched structure and a trapezoidal track device.

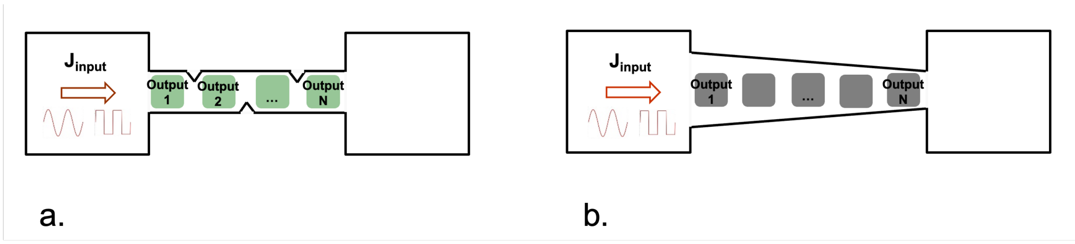

FIGURE 4.11: **New layout solutions**: a. Notches are inserted along the track to create local regions of higher current density. b. Trapezoidal track ensures a gradual increase of current density along the direction of motion.

Both of them have been fabricated during the last part of my internship and they still have to be properly tested for reservoir computing. Some preliminary tests have been performed showing a strong non-linear correlation between outputs in different positions.

Finally another solution, that can be exploited, is to aim for skyrmions instead of meander domain walls. In this optic, each skyrmion can be seen and a single neuron with a specific response. Therefore by combining all these data from a skyrmion lattice it will be possible to build up a spatial reservoir. This solution still needs to be tested and its reliability assessed.

As a future perspective, once high accuracy is achieved through improvements to the device and surrounding instrumentation, the goal will shift towards addressing more complex pattern recognition tasks, starting with handwritten digit recognition. In this case, images will be converted into a one-dimensional signal for processing, with the ultimate goal of extending the approach to spoken digit recognition. Another promising improvement involves replacing the current image-based detection system with a fully integrated device (Fig. 4.12).

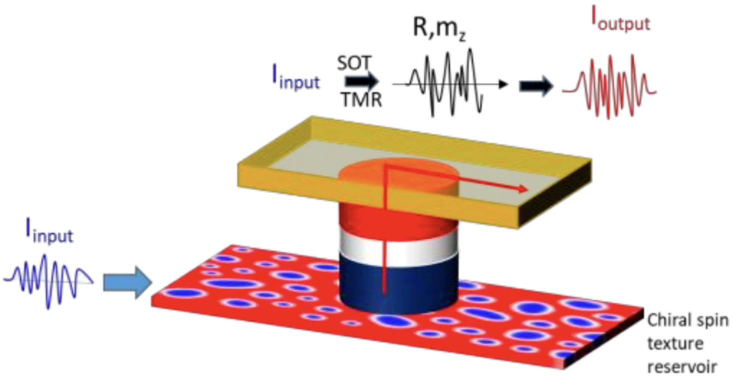

FIGURE 4.12: **Three terminal device for integrated read-out**: A new device solution is presented, featuring a magneto-tunnel junction (MTJ) nanofabricated on top of the track for fast and precise read-out. The input terminal is located at the track level, while the output is read through the MTJ contact, with the read-out signal displayed as a change in resistance.

Here, the motion of magnetic textures would be tracked electrically using magnetic tunnel junctions fabricated over the tracks. This would significantly increase read-out speed and precision, enabling faster signals with shorter periods and more information, paving the way for further advancements.

Conclusions

This study has successfully explored the potential of complex magnetic spin textures for reservoir computing by leveraging their current-induced dynamics. The properties of meander domain walls and skyrmions, specifically their micro-nano scale, nonlinearity, memory, and dynamic complexity, position them as highly promising candidates for this field.

In this research, the DC current response of an ultrathin single-wedged Ta/FeCoB/TaOx/AlOx film was analyzed using MOKE microscopy. Measurements of domain wall velocities enabled the identification of a voltage threshold value and highlighted the non-linear regime of motion, which is critical for the implementation of reservoir computing.

The study determined the optimal current density regime necessary to avoid strong deformation and excessively rapid motion. Following this, the memory properties of the system were analyzed through multiple excitations, revealing that prior excitation history significantly influences output. Notably, after applying a sinusoidal input, distinct dynamics were observed based on whether the system had previously been excited by sine or square waves. The duration of this memory effect was quantified at approximately 1.8 seconds for a 10s excitation period, showing the capacity of the system to remember past inputs and adjust its response accordingly.

With the key properties for reservoir computing verified, the study further investigated the potential of the system for simple recognition tasks, including sine/square classification. A random input sequence was applied to the system, and responses were recorded over multiple measurements. These recordings were segmented into regions representing individual neurons for optimal performance analysis. The input signals were organized into a matrix for processing, and only the final layer of the neural network was trained using linear regression. Various configurations of neurons and area subdivisions resulted in classification accuracies ranging from 60% to 70%. The observed low accuracy can be attributed to measurement noise and to the potential lack of complexity in the system, limiting reliable classification.

In conclusion, while the complex spin texture system has demonstrated its ability to function as a physical reservoir for classification tasks, enhancing recognition accuracy remains essential for reliability. New strategies are being actively explored, including variable current density along the device to induce nonlinear correlations between neurons. To this end, device layouts are being redesigned into notched and trapezoidal structures to create diverse current density distributions. Another solution involves focusing on skyrmions that may enable each skyrmion to function as a neuron, forming a spatial reservoir. Future work will involve the development of an integrated device with magnetic tunnel junctions to achieve faster and more precise readout of magnetic textures, with the goal of addressing more complex pattern recognition tasks, such as handwritten and spoken digit recognition.

Bibliography

[1] S. Chikazumi. *Physics of Ferromagnetism*. International Series of Monographs on Physics. OUP Oxford, 2009, pp. 11–12, 129–130.

[2] Aharoni A. “Demagnetizing factors for rectangular ferromagnetic prisms”. In: *Journal of Applied Physics* 83.6 (Mar. 1998), pp. 3432–3434.

[3] Roméo Juge. “Exploring different facets of magnetic skyrmion nucleation and dynamics in ultra-thin films”. PhD thesis. Université Grenoble Alpes, 2020.

[4] Stephen Blundell. *Magnetism in condensed matter*. Oxford master series in condensed matter physics. Oxford ; New York: Oxford University Press, 2001, pp. 82–83,130. 238 pp.

[5] Alex Hubert and Rudolf Schäfer. *Magnetic Domains: The Analysis of Magnetic Microstructures*. Springer Science & Business Media, Aug. 1998, pp. 106–108, 472. 1182 pp.

[6] Néel L. “Anisotropie magnétique superficielle et surstructures d’orientation”. In: *Journal de Physique et le Radium* 15.4 (1954), p. 9.

[7] Anjan Soumyanarayanan et al. “Emergent phenomena induced by spin–orbit coupling at surfaces and interfaces”. In: *Nature* 539.7630 (Nov. 2016). Publisher: Nature Publishing Group, pp. 509–517. DOI: `10.1038/nature19820`.

[8] I. Dzyaloshinsky. “A thermodynamic theory of “weak” ferromagnetism of antiferromagnetics”. In: *Journal of Physics and Chemistry of Solids* 4.4 (1958), pp. 241–255.

[9] Toru Moriya. “New Mechanism of Anisotropic Superexchange Interaction”. In: *Phys. Rev. Lett.* 4 (5 Mar. 1960), pp. 228–230.

[10] Tôru Moriya. “Anisotropic Superexchange Interaction and Weak Ferromagnetism”. In: *Phys. Rev.* 120 (1 Oct. 1960), pp. 91–98.

[11] L. Landau and E. Lifshitz. “On the theory of the dispersion of magnetic permeability in ferromagnetic bodies”. In: *Perspectives in Theoretical Physics*. Ed. by L. P. Pitaevski. Amsterdam: Pergamon, Jan. 1992, pp. 51–65. DOI: `10.1016/B978-0-08-036364-6.50008-9`.

[12] André Thiaville et al. “Dynamics of Dzyaloshinskii domain walls in ultrathin magnetic films”. In: *Europhysics Letters* 100.5 (Dec. 2012). Publisher: EDP Sciences, IOP Publishing and Società Italiana di Fisica, p. 57002.

[13] T. H. R. Skyrme. “A unified field theory of mesons and baryons”. In: *Nuclear Physics* 31 (1962), pp. 556–569. DOI: `https://doi.org/10.1016/0029-5582(62)90775-7`.

[14] Hans-Benjamin Braun. “Topological effects in nanomagnetism: from superparamagnetism to chiral quantum solitons”. In: *Advances in Physics* 61.1 (2012). Publisher: Taylor & Francis_eprint, pp. 1–116. DOI: `10.1080/00018732.2012.663070`.

[15] Naoto Nagaosa and Yoshinori Tokura. “Topological properties and dynamics of magnetic skyrmions”. In: *Nature Nanotechnology* 8.12 (Dec. 2013). Publisher: Nature Publishing Group, pp. 899–911. DOI: `10.1038/nnano.2013.243`.

[16] T.L. Gilbert. “A phenomenological theory of damping in ferromagnetic materials”. In: *IEEE Transactions on Magnetics* 40.6 (2004), pp. 3443–3449. DOI: `10.1109/TMAG.2004.836740`.

[17] O. Boulle, G. Malinowski, and M. Kläui. “Current-induced domain wall motion in nanoscale ferromagnetic elements”. In: *Materials Science and Engineering: R: Reports* 72.9 (2011), pp. 159–187. DOI: `https://doi.org/10.1016/j.mser.2011.04.001`.

[18] Vincent Baltz. *The basics of electron transport in spintronics: textbook with lectures, exercises and solutions*. EDP Sciences, May 2023, pp. 49–51. URL: `https://hal.science/hal-03716680`.

[19] M. Kläui et al. “Domain wall motion induced by spin polarized currents in ferromagnetic ring structures”. In: *Applied Physics Letters* 83.1 (July 2003), pp. 105–107. DOI: `10.1063/1.1588736`.

[20] A. Thiaville et al. “Domain wall motion by spin-polarized current: a micromagnetic study”. In: *Journal of Applied Physics* 95.11 (June 2004), pp. 7049–7051. DOI: `10.1063/1.1667804`.

[21] S. Zhang and Z. Li. “Roles of Nonequilibrium Conduction Electrons on the Magnetization Dynamics of Ferromagnets”. In: *Phys. Rev. Lett.* 93 (Sept. 2004), p. 127204. DOI: `10.1103/PhysRevLett.93.127204`.

[22] Jianwei Zhang et al. “Identification of Transverse Spin Currents in Noncollinear Magnetic Structures”. In: *Phys. Rev. Lett.* 93 (Dec. 2004), p. 256602. DOI: `10.1103/PhysRevLett.93.256602`.

[23] Ion Garate et al. “Nonadiabatic spin-transfer torque in real materials”. In: *Phys. Rev. B* 79 (Mar. 2009), p. 104416. DOI: `10.1103/PhysRevB.79.104416`.

[24] A. V. Khvalkovskiy et al. “Matching domain-wall configuration and spin-orbit torques for efficient domain-wall motion”. In: *Phys. Rev. B* 87 (Jan. 2013), p. 020402. DOI: `10.1103/PhysRevB.87.020402`.

[25] A. Manchon et al. “Current-induced spin-orbit torques in ferromagnetic and antiferromagnetic systems”. In: *Rev. Mod. Phys.* 91 (Sept. 2019), p. 035004. DOI: `10.1103/RevModPhys.91.035004`.

[26] A. A. Thiele. “Steady-State Motion of Magnetic Domains”. In: *Phys. Rev. Lett.* 30 (Feb. 1973), pp. 230–233. DOI: `10.1103/PhysRevLett.30.230`.

[27] Mathieu Riou. “Brain-inspired computing leveraging the transient non-linear dynamics of magnetic nano-oscillators”. PhD thesis. Université Paris Saclay (COmUE), Jan. 2019. URL: `https://theses.hal.science/tel-02101169`.

[28] Y. Bengio, P. Simard, and P. Frasconi. “Learning long-term dependencies with gradient descent is difficult”. In: *IEEE Transactions on Neural Networks* 5.2 (1994), pp. 157–166. DOI: `10.1109/72.279181`.

[29] Razvan Pascanu, Tomas Mikolov, and Yoshua Bengio. *On the difficulty of training recurrent neural networks*. Ed. by Sanjoy Dasgupta and David McAllester. Vol. 28. Proceedings of Machine Learning Research 3. Atlanta, Georgia, USA: PMLR, June 2013, pp. 1310–1318. URL: `https://proceedings.mlr.press/v28/pascanu13.html`.

[30] Wolfgang Maass, Thomas Natschläger, and Henry Markram. "Real-Time Computing Without Stable States: A New Framework for Neural Computation Based on Perturbations". In: *Neural computation* 14 (Dec. 2002), pp. 2531–60. DOI: `10.1162/089976602760407955`.

[31] Herbert Jaeger. "The "echo state" approach to analysing and training recurrent neural networks-with an erratum note". In: *Bonn, Germany: German National Research Center for Information Technology GMD Technical Report* 148.34 (2001), p. 13. URL: `https://www.ai.rug.nl/minds/uploads/EchoStatesTechRep.pdf`.

[32] Herbert Jaeger and Harald Haas. "Harnessing Nonlinearity: Predicting Chaotic Systems and Saving Energy in Wireless Communication". In: *Science* 304.5667 (2004), pp. 78–80. DOI: `10.1126/science.1091277`.

[33] J.J. Steil. "Backpropagation-decorrelation: online recurrent learning with O(N) complexity". In: *2004 IEEE International Joint Conference on Neural Networks (IEEE Cat. No.04CH37541)*. Vol. 2. 2004, 843–848 vol.2. DOI: `10.1109/IJCNN.2004.1380039`.

[34] Thomas M. Cover. "Geometrical and Statistical Properties of Systems of Linear Inequalities with Applications in Pattern Recognition". In: *IEEE Transactions on Electronic Computers* EC-14.3 (1965), pp. 326–334. DOI: `10.1109/PGEC.1965.264137`.

[35] Daniele Pinna, George Bourianoff, and Karin Everschor-Sitte. *Reservoir Computing with Random Skyrmion Textures*. Nov. 2018. DOI: `10.48550/arXiv.1811.12623`.

[36] Wolfgang Maass, Prashant Joshi, and Eduardo D Sontag. "Computational Aspects of Feedback in Neural Circuits". In: *PLOS Computational Biology* 3.1 (Jan. 2007), pp. 1–20. DOI: `10.1371/journal.pcbi.0020165`.

[37] L. Appeltant et al. "Information processing using a single dynamical node as complex system". In: *Nature Communications* 2.1 (Sept. 2011). Publisher: Nature Publishing Group, p. 468. ISSN: 2041-1723. DOI: `10.1038/ncomms1476`.

[38] Herbert Jaeger. *Short term memory in echo state networks*. Tech. rep. Fraunhofer Institute for Autonomous Intelligent Systems, May 2002. URL: `https://www.ai.rug.nl/minds/uploads/STMEchoStatesTechRep.pdf`.

[39] R. Penrose. "A generalized inverse for matrices". In: *Mathematical Proceedings of the Cambridge Philosophical Society* 51.3 (1955), 406–413. DOI: `10.1017/S0305004100030401`.

[40] A.N. Tikhonov. "On the solution of ill-posed problems and the method of regularization". In: *Doklady Akademii Nauk* 151 (1963), 501–504.

[41] Olivier Boulle et al. "Room-temperature chiral magnetic skyrmions in ultrathin magnetic nanostructures". In: *Nature Nanotechnology* 11.5 (May 2016), pp. 449–454. ISSN: 1748-3395. DOI: `10.1038/nnano.2015.315`.

[42] Raj Kumar et al. "Control of skyrmion chirality in Ta/FeCoB/TaO$_x$ trilayers by TaO$_x$ oxidation and FeCoB thickness". In: *Physical Review Applied* 19.2 (Feb. 2023), p. 024064. DOI: `10.1103/PhysRevApplied.19.024064`.

[43] Tomoyuki Yokouchi et al. "Pattern recognition with neuromorphic computing using magnetic field–induced dynamics of skyrmions". In: *Science Advances* 8.39 (2022). DOI: `10.1126/sciadv.abq5652`.